Received: 20 November 2017 | Revised: 15 January 2018 | Accepted: 16 January 2018

DOI: 10.1002/nme.5771

RESEARCH ARTICLE

WILEY

High-performance geometric nonlinear analysis with the unsymmetric 4-node, 8-DOF plane element US-ATFQ4

Zhi Li[1] | Song Cen[1,2] | Cheng-Jin Wu[1] | Yan Shang[3] | Chen-Feng Li[4]

[1]Department of Engineering Mechanics, School of Aerospace Engineering, Tsinghua University, Beijing, China

[2]Key Laboratory of Applied Mechanics, School of Aerospace Engineering, Tsinghua University, Beijing, China

[3]State Key Laboratory of Mechanics and Control of Mechanical Structures, College of Aerospace Engineering, Nanjing University of Aeronautics and Astronautics, Nanjing, China

[4]College of Engineering, Swansea University, Swansea, UK

Correspondence
Song Cen, Department of Engineering Mechanics, School of Aerospace Engineering, Tsinghua University, Beijing 100084, China.
Email: censong@tsinghua.edu.cn

Funding information
National Natural Science Foundation of China, Grant/Award Number: 11272181 and 11702133; Tsinghua University Initiative Scientific Research Program, Grant/Award Number: 2014z09099; Natural Science Foundation of Jiangsu Province, Grant/Award Number: BK20170772

Summary

A recent unsymmetric 4-node, 8-DOF plane element US-ATFQ4, which exhibits excellent precision and distortion-resistance for linear elastic problems, is extended to geometric nonlinear analysis. Since the original linear element US-ATFQ4 contains the analytical solutions for plane pure bending, how to modify such formulae into incremental forms for nonlinear applications and design an appropriate updated algorithm become the key of the whole job. First, the analytical trial functions should be updated at each iterative step in the framework of updated Lagrangian formulation that takes the configuration at the beginning of an incremental step as the reference configuration during that step. Second, an appropriate stress update algorithm in which the Cauchy stresses are updated by the Hughes-Winget method is adopted to estimate current stress fields. Numerical examples show that the new nonlinear element US-ATFQ4 also possesses amazing performance for geometric nonlinear analysis, no matter whether regular or distorted meshes are used. It again demonstrates the advantages of the unsymmetric finite element method with analytical trial functions.

KEYWORDS

analytical trial function, finite element, geometric nonlinear analysis, mesh distortion, UL formulation, unsymmetric 4-node plane element

1 | INTRODUCTION

The traditional 4-node, 8-DOF isoparametric element with full integration scheme, denoted by Q4, is one of the most popular models adopted for 2-dimensional (2D) finite element analysis. However, in many high-order problems, this model exhibits an over-stiff behavior and suffers from various locking problems, and this situation will become worse if distorted meshes are used.[1,2] In order to improve the performance of element Q4, some researchers developed incompatible models, such as the element Q6 proposed by Wilson et al[3] and its modified version QM6 proposed by Taylor et al,[4] and the Abaqus incompatible elements CPS4I/CPE4I[5] with assumed strains.[6] Although these incompatible models have reliable performance for regular meshes generally, they are still sensitive to mesh distortion and will lose most precision in distorted meshes. Reduced integration scheme was also suggested to resist over-stiff and sensitive problems to mesh distortion. Nevertheless, it may deteriorate the precision for stresses and bring *hourglass* problem (over-soft).[5] During the past decades, numerous efforts have been made to look for robust 4-node, 8-DOF quadrilateral element models.

In addition to the aforementioned incompatible and reduced integration schemes, some other techniques, including the hybrid stress method,[7-12] the quasi-conforming method,[13] the generalized conforming method,[2] the improved enhanced strain method,[14-16] the B-bar method,[17] the quadrilateral area coordinate method,[18-27] etc, can be found in related references. Although these models can improve the performance more or less, the sensitivity problem to mesh distortion has never been overcome from the outset. Especially, no element can overcome the obstacle stipulated by MacNeal's theorem,[28,29] ie, any 4-node, 8-DOF plane membrane element will either lock in in-plane bending or fail to pass a C_0 patch test when the element's shape is an isosceles trapezoid, which means such elements must be sensitive to mesh distortions.

Recently, Cen et al[30] developed an unsymmetric 4-node, 8-DOF plane element US-ATFQ4 based on the virtual work principle.[31] In the formulations of element US-ATFQ4, 2 different sets of shape functions are simultaneously used. The first set that comes from the traditional 4-node bilinear isoparametric element Q4 is employed as test functions, whereas the second set, which is employed as trial functions, uses analytical solutions for plane pure bending in terms of the second form of quadrilateral area coordinates (QACM-II) (S, T).[24] This element exhibits excellent performance in rigorous tests and successfully breaks through the limitation defined by MacNeal's theorem,[28,29] that it to say, it is insensitive to various serious mesh distortions.

Actually, since mesh distortions will appear more easily because of large strains, or large displacements, or large rotations, a distortion-resistance finite element model should be more valuable in nonlinear analysis. For geometric nonlinear problems, there are usually 3 Lagrangian kinematic descriptions for finite element analysis,[32] including total Lagrangian formulation, updated Lagrangian (UL) formulation, and corotational formulation. The total Lagrangian formulation requires that all quantities are referred to the original, undeformed configuration, whereas the UL formulation takes the current configuration, ie, the configuration at the beginning of an incremental step, as the reference configuration during that step. In the corotational formulation, the displacements and rotations are allowed to be arbitrarily large, but strains are limited to be small. Among these 3 formulations, the UL formulation is often preferred because it possesses better flexibility for solving various complicated nonlinear problems. Usually, it adopts the concept of Cauchy (physical) stress and uses the rate-of-deformation as a measure of stain rate, but other measures of strain or strain rate can also be used.[33] Furthermore, a procedure for evaluating current stresses is required in the implementation of the UL formulation, and a so-called incrementally objective stress update scheme that can exactly account for the proper rotation of the stresses in a rigid body rotation for large deformation problems is needed. Hughes and Winget[34] introduced the concept of incremental objectivity, and Rashid[35] further distinguished it into weak objectivity and strong objectivity. Subsequently, Simo and Hughes[36] gave an extensive discussion on the incrementally objective stress update algorithms based on the concept of Lie derivatives.

Recently, new displacement-based 4-node, 8-DOF plane quadrilateral finite element models for analysis of geometric nonlinear problems can still be found in various literary works such as the nonlinear quadrilateral area coordinate element AGQ6-I,[23] the nonlinear quasi-conforming element,[37] and the nonlinear assumed strain MITC element.[38] However, as previously mentioned, no model can break MacNeal's theorem so that their performances cannot be guaranteed when severely distorted mesh appears. Some researchers hoped to solve this difficulty by introducing other new techniques such as the 4-node Hu-Washizu elements based on skew coordinates presented by Wisniewski et al,[39,40] the elements with the additional rotational DOF presented by Zouari et al,[41] the hybrid discontinuous Galerkin method proposed by Wulfinghoff et al,[42] and the partition of unity-based "FE-meshfree" method proposed by Rajendran et al.[43] Nevertheless, the computation costs also increase at the same time.

It is very interesting that whether the unsymmetric element US-ATFQ4,[30] which possesses high distortion-resistance for linear elastic problems, can be extended to nonlinear applications. However, some researchers negate this extension, they think that the approach, which employs the analytical solutions satisfying all governing equations for linear elasticity, restricts the element to linear elastic analysis.[44] In fact, the analytical trial functions are only the functions of physical coordinates with material constants. These coordinates and material constants can be updated referring to the current configuration at each iterative step so that it is possible to use them as part of the incremental equations of the UL formulation.

The main purpose of this paper is to extend the 4-node, 8-DOF unsymmetric element US-ATFQ4 to the geometric nonlinear analysis. Since the original linear element US-ATFQ4 contains the analytical solutions for plane pure bending, how to modify such formulae into incremental forms for nonlinear applications and design an appropriate updated algorithm become the key of the whole job. As many engineering materials still present small strain state in practice,[45] this paper will only focus on small strain with large displacement/rotation problems. The content of the work is organized as follows. In Section 2, the UL formulation is briefly reviewed. In Section 3, the formulations of element US-ATFQ4 for geometric nonlinear analysis are established, and the numerical implementation in Abaqus user element (UEL) subroutine[5] is

also introduced. In the following Section 4, several typical geometric nonlinear numerical examples are employed to test the performance of the present formulations. It can be seen that the proposed nonlinear element US-ATFQ4 can provide excellent results in both regular and distorted meshes, which demonstrates the advantages of the new unsymmetric finite element method with linear analytical trial functions.

2 | BRIEF REVIEW ON THE UPDATED LAGRANGIAN FORMULATION

As shown in Figure 1, a general deformable body experiencing large displacement motion in the Cartesian coordinate system is considered. C_0, C_1, and C_2 are the configurations of the body at times 0, t, and $t+\Delta t$, respectively. The Cartesian coordinates of a point P within the body at these 3 different configurations are $({}^0x, {}^0y, {}^0z)$, $({}^tx, {}^ty, {}^tz)$, and $({}^{t+\Delta t}x, {}^{t+\Delta t}y, {}^{t+\Delta t}z)$, respectively, in which the left superscripts refer to the times for 3 different configurations of the body. Therefore, the displacement increments are given by $u_i = {}^{t+\Delta t}x_i - {}^tx_i,\ (i = 1, 2, 3)$. Note: 2 types of notation, ie, indicial notation and matrix notation, are both used in this paper. In order to avoid confusion with nodal values, the Cartesian coordinates are expressed by (x, y, z), rather than the form with subscripts, ie, $x_1 = x,\ x_2 = y$, and $x_3 = z$. For the components of a vector, their subscripts are also expressed by (x, y, z), rather than $(1, 2, 3)$; for example, the components of the displacement increments u_i in 3 dimensions are $u_1 = u_x,\ u_2 = u_y$, and $u_3 = u_z$. The nodal indices are indicated by upper case letters; for example, u_{iI} is the i-component of the displacement increments at node I.[33] In conformance with the rules of Einstein notation, indices repeated twice in a term should be summed.

In the UL formulation, the equilibrium equation of the body at time $t+\Delta t$ referring to configuration C_1 can be derived by the principle of virtual displacements and expressed by[46]

$$\int_{t_V} {}^{t+\Delta t}_{t}S_{ij}\delta\, {}^{t+\Delta t}_{t}\varepsilon_{ij}\,\mathrm{d}^tV - \left(\int_{t_V} {}^{t+\Delta t}_{t}f_i\delta u_i\,\mathrm{d}^tV + \int_{t_S} {}^{t+\Delta t}_{t}t_i\delta u_i\,\mathrm{d}^tS\right) = 0, \tag{1}$$

where ${}^{t+\Delta t}_{t}S_{ij}$ and ${}^{t+\Delta t}_{t}\varepsilon_{ij}$ denote, respectively, the second Piola-Kirchoff stress tensor and the Green-Lagrange strain tensor, which are defined at time $t+\Delta t$ and referred to configuration C_1; and

$$\int_{t_V} {}^{t+\Delta t}_{t}f_i\delta u_i\,\mathrm{d}^tV + \int_{t_S} {}^{t+\Delta t}_{t}t_i\delta u_i\,\mathrm{d}^tS = \delta^{t+\Delta t}W_{ext}, \tag{2}$$

where $\delta^{t+\Delta t}W_{ext}$ denotes the external virtual work at time $t+\Delta t$; ${}^{t+\Delta t}_{t}f_i$ and ${}^{t+\Delta t}_{t}t_i$ denote, respectively, the components of the body force vector and the boundary traction vector applied to configuration C_2 and referred to configuration C_1; δu_i denotes virtual displacement vector imposed on configuration C_2; and ${}^tV$ and ${}^tS$ denote the volume and the surface area of the body under discussion referred to configuration C_1, respectively.

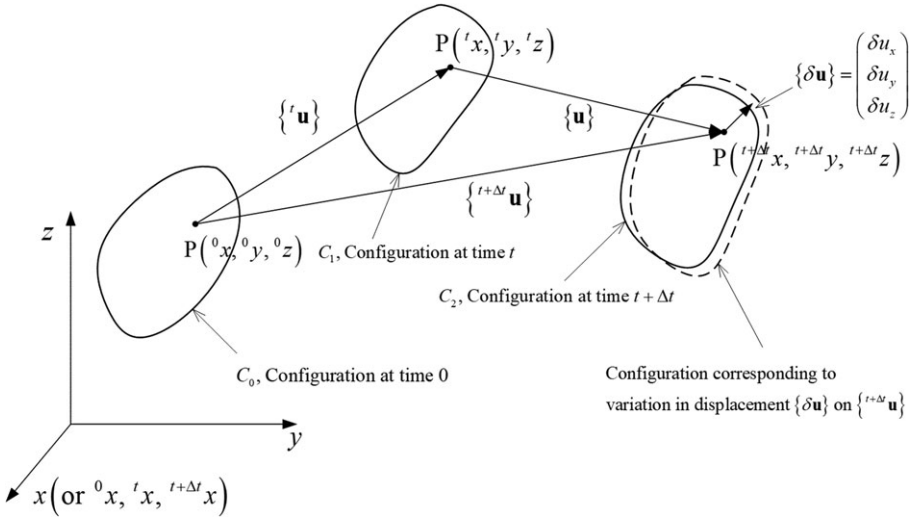

FIGURE 1 Large displacement motion of a body in Cartesian coordinate system

Equation (1) is a nonlinear equation for solving the displacement increments u_i. In order to make it computationally tractable, Equation (1) is usually linearized by introducing the following relations and approximations[46]:

$$ {}^{t+\Delta t}_{t}S_{ij} = {}^{t}\sigma_{ij} + {}_{i}S_{ij}, \left({}^{t}_{t}S_{ij} \equiv {}^{t}\sigma_{ij}\right), \tag{3} $$

$$ \begin{cases} {}^{t+\Delta t}_{t}\varepsilon_{ij} = {}_{t}\varepsilon_{ij} = {}_{t}e_{ij} + {}_{t}\eta_{ij} \\ {}_{t}e_{ij} = \frac{1}{2}\left({}_{t}u_{i,j} + {}_{t}u_{i,j}\right); {}_{t}\eta_{ij} = \frac{1}{2}{}_{t}u_{k,i}{}_{t}u_{k,j}, \end{cases} \tag{4} $$

$$ {}_{t}S_{ij} = {}_{t}C_{ijrs}{}_{t}e_{rs}; \delta_{t}\varepsilon_{ij} = \delta_{t}e_{ij}, \tag{5} $$

where ${}^{t}\sigma_{ij}$ are the components of the known Cauchy stresses at time t; ${}_{t}e_{ij}$ and ${}_{t}\eta_{ij}$ are the linear and nonlinear incremental strains referred to configuration C_1, respectively; ${}_{t}u_{i,j} = \frac{\partial u_i}{\partial {}^{t}x_j}$ are the derivatives of the displacement increments u_i referring to the coordinates ${}^{t}x_j$; and ${}_{t}C_{ijrs}$ are the components of the incremental stress-strain relation tensor at time t referred to configuration C_1.

Substitution of Equations (3), (4), and (5) into Equation (1) yields the linearized equilibrium equation

$$ \int_{{}^{t}V} {}_{t}C_{ijrs}{}_{t}e_{rs}\delta_{t}e_{ij}\mathrm{d}{}^{t}V = \int_{{}^{t}V} {}^{t}\sigma_{ij}\delta_{t}\eta_{ij}\mathrm{d}{}^{t}V = \delta^{t+\Delta t}W_{ext} - \int_{{}^{t}V} {}^{t}\sigma_{ij}\delta_{t}e_{ij}\mathrm{d}{}^{t}V. \tag{6} $$

3 | EXTENSION OF THE UNSYMMETRIC 4-NODE, 8-DOF PLANE ELEMENT US-ATFQ4 FOR GEOMETRIC NONLINEAR ANALYSIS

3.1 | Geometric nonlinear formulations for element US-ATFQ4

In this section, the unsymmetric 4-node plane membrane element US-ATFQ4,[30] which can perfectly break through MacNeal's theorem[28,29] and possesses excellent distortion-resistance for linear elasticity,[30] is extended to applications for geometric nonlinear problems.

A 4-node, 8-DOF plane quadrilateral element is shown in Figure 2. Nodes 1, 2, 3, and 4 are the corner nodes; $({}^{t}x_I, {}^{t}y_I)$ and $({}^{t}S_I, {}^{t}T_I)$ are respectively the Cartesian coordinates and quadrilateral area coordinates (QACM-II)[24] (see Appendix A) of the corner node I ($I = 1, 2, 3, 4$) at time t; and $u_{\alpha I}$ is the α-component ($\alpha = 1, 2$) of the displacement increments at node I. For the unsymmetric element US-ATFQ4,[30] 2 different sets of interpolation functions for displacement fields are simultaneously used. The first set is for the virtual displacement fields $\{\delta\mathbf{u}\}$ and employs the shape functions of the traditional 4-node bilinear isoparametric element, ie,

$$ \{\delta\mathbf{u}\} = \begin{Bmatrix} \delta u_x \\ \delta u_y \end{Bmatrix} = \left[\overline{\mathbf{N}}\right]\left\{\delta\Delta\mathbf{q}^e\right\}, \tag{7} $$

where

$$ \left\{\delta\Delta\mathbf{q}^e\right\} = \left[\delta u_{x1}\ \ \delta u_{y1}\ \ \delta u_{x2}\ \ \delta u_{y2}\ \ \delta u_{x3}\ \ \delta u_{y3}\ \ \delta u_{x4}\ \ \delta u_{y4}\right]^{\mathrm{T}}, \tag{8} $$

$$ \left[\overline{\mathbf{N}}\right] = \begin{bmatrix} \overline{N}_1 & 0 & \overline{N}_2 & 0 & \overline{N}_3 & 0 & \overline{N}_4 & 0 \\ 0 & \overline{N}_1 & 0 & \overline{N}_2 & 0 & \overline{N}_3 & 0 & \overline{N}_4 \end{bmatrix}, \tag{9} $$

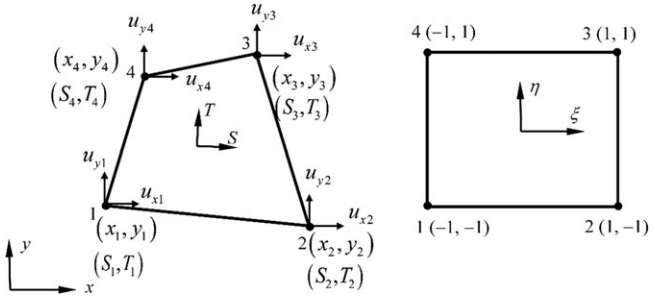

FIGURE 2 A 4-node plane quadrilateral element

with

$$\overline{N}_I = \frac{1}{4}(1+\xi_I\xi)(1+\eta_I\eta), \qquad (I=1,2,3,4). \tag{10}$$

Furthermore, $\{\delta\Delta\mathbf{q}^e\}$ is the nodal virtual displacement vector, $[\overline{\mathbf{N}}]$ is the interpolation function matrix of traditional 4-node bilinear isoparametric element, and (ξ_I, η_I) are the nodal isoparametric coordinates.

The second set is for the real incremental displacement fields $\{\mathbf{u}\}$ and adopts a composite coordinate interpolation scheme with analytical trial functions

$$\{\mathbf{u}\} = \begin{Bmatrix} u_x \\ u_y \end{Bmatrix} = [\mathbf{P}]\{\boldsymbol{\alpha}\} = \begin{bmatrix} 1 & 0 & {}^tx & 0 & {}^ty & 0 & {}^tU_7 & {}^tU_8 \\ 0 & 1 & 0 & {}^tx & 0 & {}^ty & {}^tV_7 & {}^tV_8 \end{bmatrix} \begin{Bmatrix} \alpha_1 \\ \alpha_2 \\ \alpha_3 \\ \vdots \\ \alpha_8 \end{Bmatrix}, \tag{11}$$

where α_i $(i = 1 \sim 8)$ are 8 undetermined coefficients; ${}^tU_7$, ${}^tV_7$, ${}^tU_8$, and ${}^tU_8$ are the linear displacement solutions for plane pure bending in arbitrary direction and in terms of the second form of quadrilateral area coordinates (QACM-II) (S, T)[24] (see Appendix A) at time t. The detailed expressions of ${}^tU_7$, ${}^tV_7$, ${}^tU_8$, and ${}^tU_8$ are derived in the work of Cen et al[30] and given in Appendix B. Substitution of nodal coordinates (including Cartesian and QACM-II) and nodal displacement increments into Equation (11) yields

$$\{\mathbf{u}\} = \begin{Bmatrix} u_x \\ u_y \end{Bmatrix} = \left[{}^t\hat{\mathbf{N}}\right]\left\{\Delta\mathbf{q}^e\right\}, \tag{12}$$

where

$$\left\{\Delta\mathbf{q}^e\right\} = \left[\, u_{x1} \;\; u_{y1} \;\; u_{x2} \;\; u_{y2} \;\; u_{x3} \;\; u_{y3} \;\; u_{x4} \;\; u_{y4} \,\right]^{\mathrm{T}}, \tag{13}$$

$$\left[{}^t\hat{\mathbf{N}}\right] = \begin{bmatrix} {}^t\hat{N}_{11} & {}^t\hat{N}_{12} & {}^t\hat{N}_{13} & {}^t\hat{N}_{14} & {}^t\hat{N}_{15} & {}^t\hat{N}_{16} & {}^t\hat{N}_{17} & {}^t\hat{N}_{18} \\ {}^t\hat{N}_{21} & {}^t\hat{N}_{22} & {}^t\hat{N}_{23} & {}^t\hat{N}_{24} & {}^t\hat{N}_{25} & {}^t\hat{N}_{26} & {}^t\hat{N}_{27} & {}^t\hat{N}_{28} \end{bmatrix}. \tag{14}$$

In addition, $\{\Delta\mathbf{q}^e\}$ is the nodal displacement increment vector and $\left[{}^t\hat{\mathbf{N}}\right]$ is the composite coordinate interpolation functions matrix. The detailed expressions of $\left[{}^t\hat{\mathbf{N}}\right]$ are given in Appendix B. It can be seen that the interpolation functions matrix $\left[{}^t\hat{\mathbf{N}}\right]$ depends on current coordinates; therefore, the analytical trial functions should be updated at each iterative step in the framework of updated Lagrangian formulation.

The first term at the left side of Equation (6) can be rewritten in the following matrix form:

$$\begin{aligned} &\int_{{}^tV} {}^tC_{ijrs}\,{}^te_{rs}\delta_t e_{ij}\,\mathrm{d}^tV \\ &= \sum_e \int_{{}^tV_e} \begin{Bmatrix} \delta_t u_{x,x} \\ \delta_t u_{y,y} \\ \delta_t u_{x,y} + \delta_t u_{y,x} \end{Bmatrix}^{\mathrm{T}} \begin{bmatrix} {}^tC_{11} & {}^tC_{12} & {}^tC_{16} \\ {}^tC_{21} & {}^tC_{22} & {}^tC_{26} \\ {}^tC_{61} & {}^tC_{62} & {}^tC_{66} \end{bmatrix} \begin{Bmatrix} {}^tu_{x,x} \\ {}^tu_{y,y} \\ {}^tu_{x,y} + {}^tu_{y,x} \end{Bmatrix} d^tV, \\ &= \sum_e \int_{{}^tV_e} \{\delta\Delta\mathbf{q}^e\}^{\mathrm{T}} \left[{}^t_t\overline{\mathbf{B}}_L\right]^{\mathrm{T}} [{}_t\mathbf{C}] \left[{}^t_t\hat{\mathbf{B}}_L\right] \{\Delta\mathbf{q}^e\}\,\mathrm{d}^tV \end{aligned} \tag{15}$$

where

$$\left[{}^t_t\overline{\mathbf{B}}_L\right] = \begin{bmatrix} {}^t\overline{N}_{1,x} & 0 & \cdots & {}^t\overline{N}_{4,x} & 0 \\ 0 & {}^t\overline{N}_{1,y} & \cdots & 0 & {}^t\overline{N}_{4,y} \\ {}^t\overline{N}_{1,y} & {}^t\overline{N}_{1,x} & \cdots & {}^t\overline{N}_{4,y} & {}^t\overline{N}_{4,x} \end{bmatrix}, \tag{16}$$

$$\left[{}^t_t\hat{\mathbf{B}}_L\right] = \begin{bmatrix} {}^t_t\hat{N}_{11,x} & {}^t_t\hat{N}_{12,x} & \cdots & {}^t_t\hat{N}_{17,x} & {}^t_t\hat{N}_{18,x} \\ {}^t_t\hat{N}_{21,y} & {}^t_t\hat{N}_{22,y} & \cdots & {}^t_t\hat{N}_{27,y} & {}^t_t\hat{N}_{28,y} \\ {}^t_t\hat{N}_{11,y} + {}^t_t\hat{N}_{21,x} & {}^t_t\hat{N}_{12,y} + {}^t_t\hat{N}_{22,x} & \cdots & {}^t_t\hat{N}_{17,y} + {}^t_t\hat{N}_{27,x} & {}^t_t\hat{N}_{18,y} + {}^t_t\hat{N}_{28,x} \end{bmatrix} \{\mathbf{u}\}. \tag{17}$$

The second term at the left side of Equation (6) can be rewritten as

$$\begin{aligned}\int_{t_V} {}^t\sigma_{ij}\delta_t\eta_{ij}\mathrm{d}^tV &= \sum_e \int_{t_{V_e}} \left[{}^t\sigma_{xx}\left(\delta u_{x,x}u_{x,x}+\delta u_{y,x}u_{y,x}\right)+{}^t\sigma_{yy}\left(\delta u_{x,y}u_{x,y}+\delta u_{y,y}u_{y,y}\right)\right.\\ &\left.+{}^t\sigma_{xy}\left(\delta u_{x,x}u_{x,y}+\delta u_{y,x}u_{y,y}+\delta u_{x,y}u_{x,x}+\delta u_{y,y}u_{y,x}\right)\right]\mathrm{d}^tV\\ &= \sum_e \int_{{}^tV_e} \begin{Bmatrix}\delta u_{x,x}\\ \delta u_{x,y}\\ \delta u_{y,x}\\ \delta u_{y,y}\end{Bmatrix}^{\mathrm{T}} \begin{bmatrix}{}^t\sigma_{xx} & {}^t\sigma_{xy} & 0 & 0\\ {}^t\sigma_{yx} & {}^t\sigma_{yy} & 0 & 0\\ 0 & 0 & {}^t\sigma_{xx} & {}^t\sigma_{xy}\\ 0 & 0 & {}^t\sigma_{yx} & {}^t\sigma_{yy}\end{bmatrix} \begin{Bmatrix}u_{x,x}\\ u_{x,y}\\ u_{y,x}\\ u_{y,y}\end{Bmatrix}\mathrm{d}^tV\\ &= \sum_e \int_{{}^tV_e} \left\{\delta\Delta\mathbf{q}^e\right\}^{\mathrm{T}}\left[{}^t_t\overline{\mathbf{B}}_{NL}\right]^{\mathrm{T}}\left[{}^t\breve{\boldsymbol{\sigma}}\right]\left[{}^t_t\hat{\mathbf{B}}_{NL}\right]\left\{\Delta\mathbf{q}^e\right\}\mathrm{d}^tV,\end{aligned} \tag{18}$$

where

$$\left[{}^t_t\overline{\mathbf{B}}_{NL}\right] = \begin{bmatrix} {}_t\overline{N}_{1,x} & 0 & \cdots & {}_t\overline{N}_{4,x} & 0\\ {}_t\overline{N}_{1,y} & 0 & \cdots & {}_t\overline{N}_{4,y} & 0\\ 0 & {}_t\overline{N}_{1,x} & \cdots & 0 & {}_t\overline{N}_{4,x}\\ 0 & {}_t\overline{N}_{1,y} & \cdots & 0 & {}_t\overline{N}_{4,y}\end{bmatrix}, \tag{19}$$

$$\left[{}^t_t\hat{\mathbf{B}}_{NL}\right] = \begin{bmatrix} {}^t_t\hat{N}_{11,x} & {}^t_t\hat{N}_{12,x} & \cdots & {}^t_t\hat{N}_{17,x} & {}^t_t\hat{N}_{18,x}\\ {}^t_t\hat{N}_{11,y} & {}^t_t\hat{N}_{12,y} & \cdots & {}^t_t\hat{N}_{17,y} & {}^t_t\hat{N}_{18,y}\\ {}^t_t\hat{N}_{21,x} & {}^t_t\hat{N}_{22,x} & \cdots & {}^t_t\hat{N}_{27,x} & {}^t_t\hat{N}_{28,x}\\ {}^t_t\hat{N}_{21,y} & {}^t_t\hat{N}_{22,y} & \cdots & {}^t_t\hat{N}_{27,y} & {}^t_t\hat{N}_{28,y}\end{bmatrix}. \tag{20}$$

The last term at the right side of Equation (6) can be rewritten as

$$\begin{aligned}\int_{{}^tV} {}^t\sigma_{ij}\delta_t e_{ij}\mathrm{d}^tV &= \sum_e \int_{{}^tV_e} \begin{Bmatrix}\delta_t e_{xx}\\ \delta_t e_{yy}\\ 2\delta_t e_{xy}\end{Bmatrix}^{\mathrm{T}} \begin{Bmatrix}{}^t\sigma_{xx}\\ {}^t\sigma_{yy}\\ {}^t\sigma_{xy}\end{Bmatrix}\mathrm{d}^tV\\ &= \sum_e \int_{{}^tV_e} \{\delta_t\mathbf{e}\}^{\mathrm{T}}\left\{{}^t\tilde{\boldsymbol{\sigma}}\right\}\mathrm{d}^tV = \sum_e \int_{{}^tV_e} \left\{\delta\Delta\mathbf{q}^e\right\}^{\mathrm{T}}\left[{}^t_t\overline{\mathbf{B}}_L\right]^{\mathrm{T}}\left\{{}^t\tilde{\boldsymbol{\sigma}}\right\}\mathrm{d}^tV.\end{aligned} \tag{21}$$

Thus, from Equations (15)-(21), Equation (6) can be expressed in the following matrix form:

$$\begin{aligned}&\sum_e \int_{t_{V_e}} \left\{\delta\Delta\mathbf{q}^e\right\}^{\mathrm{T}}\left[{}^t_t\overline{\mathbf{B}}_L\right]^{\mathrm{T}}\left[{}_t\mathbf{C}\right]\left[{}^t_t\hat{\mathbf{B}}_L\right]^{\mathrm{T}}\left\{\Delta\mathbf{q}^e\right\}d^tV + \sum_e \int_{t_{V_e}} \left\{\delta\Delta\mathbf{q}^e\right\}^{\mathrm{T}}\left[{}^t_t\overline{\mathbf{B}}_{\mathrm{NL}}\right]^{\mathrm{T}}\left[{}^t\breve{\boldsymbol{\sigma}}\right]\left[{}^t_t\hat{\mathbf{B}}_{\mathrm{NL}}\right]\left\{\Delta\mathbf{q}^e\right\}\mathrm{d}^tV\\ &= \sum_e \left\{\delta\Delta\mathbf{q}^e\right\}^{\mathrm{T}}\left\{{}^{t+\Delta t}_t\mathbf{F}^e_{ext}\right\} - \sum_e \int_{t_{V_e}} \left\{\delta\Delta\mathbf{q}^e\right\}^{\mathrm{T}}\left[{}^t_t\overline{\mathbf{B}}_L\right]^{\mathrm{T}}\left\{{}^t\tilde{\boldsymbol{\sigma}}\right\}\mathrm{d}^tV.\end{aligned} \tag{22}$$

Since $\{\delta\Delta\mathbf{q}^e\}$ in the aforementioned equation are arbitrary, the following finite element equations can be obtained:

$$\sum_e \left[{}^t_t\mathbf{K}^e_T\right]\left\{\Delta\mathbf{q}^e\right\} = \sum_e \left\{{}^{t+\Delta t}_t\mathbf{R}^e\right\}, \tag{23}$$

where

$$\left[{}^t_t\mathbf{K}^e_T\right] = \left[{}^t_t\mathbf{K}^e_L\right] + \left[{}^t_t\mathbf{K}^e_{NL}\right] \tag{24}$$

$$\left\{{}^{t+\Delta t}_t\mathbf{R}^e\right\} = \left\{{}^{t+\Delta t}_t\mathbf{F}^e_{ext}\right\} - \left\{{}^t_t\mathbf{F}^e_{int}\right\}, \tag{25}$$

$$\left[{}^t_t\mathbf{K}^e_L\right] = \int_{t_{V_e}} \left[{}^t_t\overline{\mathbf{B}}_L\right]^{\mathrm{T}}\left[{}_t\mathbf{C}\right]\left[{}^t_t\hat{\mathbf{B}}_L\right]\mathrm{d}^tV, \tag{26}$$

$$\left[{}^t_t\mathbf{K}^e_{NL}\right] = \int_{t_{V_e}} \left[{}^t_t\overline{\mathbf{B}}_{NL}\right]^{\mathrm{T}}\left[{}^t\breve{\boldsymbol{\sigma}}\right]\left[{}^t_t\hat{\mathbf{B}}_{NL}\right]\mathrm{d}^tV \tag{27}$$

$$\left\{{}^{t+\Delta t}_t\mathbf{F}^e_{ext}\right\} = \int_{t_{V_e}} \left[\overline{\mathbf{N}}\right]^{\mathbf{T}}\left\{{}^{t+\Delta t}_t\mathbf{f}\right\}\mathrm{d}^tV + \int_{t_{S_e}} \left[\overline{\mathbf{N}}\right]^{\mathbf{T}}\left\{{}^{t+\Delta t}_t\mathbf{t}\right\}\mathrm{d}^tS, \tag{28}$$

$$\left\{{}^t_t\mathbf{F}^e_{int}\right\} = \int_{t_{V_e}} \left[{}^t_t\overline{\mathbf{B}}_L\right]^{\mathrm{T}}\left\{{}^t\tilde{\boldsymbol{\sigma}}\right\}\mathrm{d}^tV. \tag{29}$$

The increments of the nodal displacements from time t to $t+\Delta t$, $\{\Delta\mathbf{q}^e\}$, can be obtained by solving Equation (23). Usually, $\{\Delta\mathbf{q}^e\}$ will be used to update the displacements, strains, and stresses at time $t+\Delta t$. Here, in order to obtain the values of Cauchy stress efficiently and accurately, instead of the usual strategy, the Hughes-Winget method[34] is adopted to update the stresses at time $t+\Delta t$, ie,

$$\left[{}^{t+\Delta t}\boldsymbol{\sigma}\right] = [\Delta\mathbf{R}]\left[{}^{t}\boldsymbol{\sigma}\right][\Delta\mathbf{R}]^{\mathrm{T}} + [\Delta\boldsymbol{\sigma}], \tag{30}$$

where

$$\left[{}^{t+\Delta t}\boldsymbol{\sigma}\right] = \begin{bmatrix} {}^{t+\Delta t}\sigma_{xx} & {}^{t+\Delta t}\sigma_{xy} \\ {}^{t+\Delta t}\sigma_{yx} & {}^{t+\Delta t}\sigma_{yy} \end{bmatrix}; [\Delta\boldsymbol{\sigma}] = \begin{bmatrix} \Delta\sigma_{xx} & \Delta\sigma_{xy} \\ \Delta\sigma_{yx} & \Delta\sigma_{yy} \end{bmatrix}, \tag{31}$$

$$\begin{aligned} [\Delta\mathbf{R}] &= \begin{bmatrix} \Delta R_{xx} & \Delta R_{xy} \\ \Delta R_{yx} & \Delta R_{yy} \end{bmatrix} = \left[\mathbf{I} - \frac{1}{2}\Delta\mathbf{W}\right]^{-1}\left[\mathbf{I} + \frac{1}{2}\Delta\mathbf{W}\right], [\mathbf{I}] = \begin{bmatrix} 1 & 0 \\ 0 & 1 \end{bmatrix}, \\ [\Delta\mathbf{W}] &= \begin{bmatrix} \Delta W_{xx} & \Delta W_{xy} \\ \Delta W_{yx} & \Delta W_{yy} \end{bmatrix}, \end{aligned} \tag{32}$$

with

$$\Delta W_{\alpha\beta} = \frac{1}{2}\left({}_{t+\Delta t/2}u_{\alpha,\beta} - {}_{t+\Delta t/2}u_{\beta,\alpha}\right), \tag{33}$$

$${}_{t+\Delta t/2}u_{\alpha,\beta} = \frac{\partial u_\alpha}{\partial {}^{t+\Delta t/2}x_\beta}; {}^{t+\Delta t/2}x_\beta = \frac{1}{2}\left({}^{t}x_\beta + {}^{t+\Delta t}x_\beta\right), \quad (\alpha,\beta = 1,2). \tag{34}$$

$\Delta W_{\alpha\beta}$, which are defined at the midpoint of the time interval, are the increments in spin; $\Delta R_{\alpha\beta}$ are the increments in rotation; and the subscripts t and $t+\Delta t$, respectively, refer to the beginning and the end of the increment.

For the isotropic elastic case, we have

$$\begin{Bmatrix} \Delta\sigma_{xx} \\ \Delta\sigma_{yy} \\ \Delta\sigma_{xy} \end{Bmatrix} = \frac{E'}{1-\mu'^2}\begin{bmatrix} 1 & \mu' & 0 \\ \mu' & 1 & 0 \\ 0 & 0 & \frac{1-\mu'}{2} \end{bmatrix}\begin{Bmatrix} \Delta D_{xx} \\ \Delta D_{yy} \\ 2\Delta D_{xy} \end{Bmatrix}, \tag{35}$$

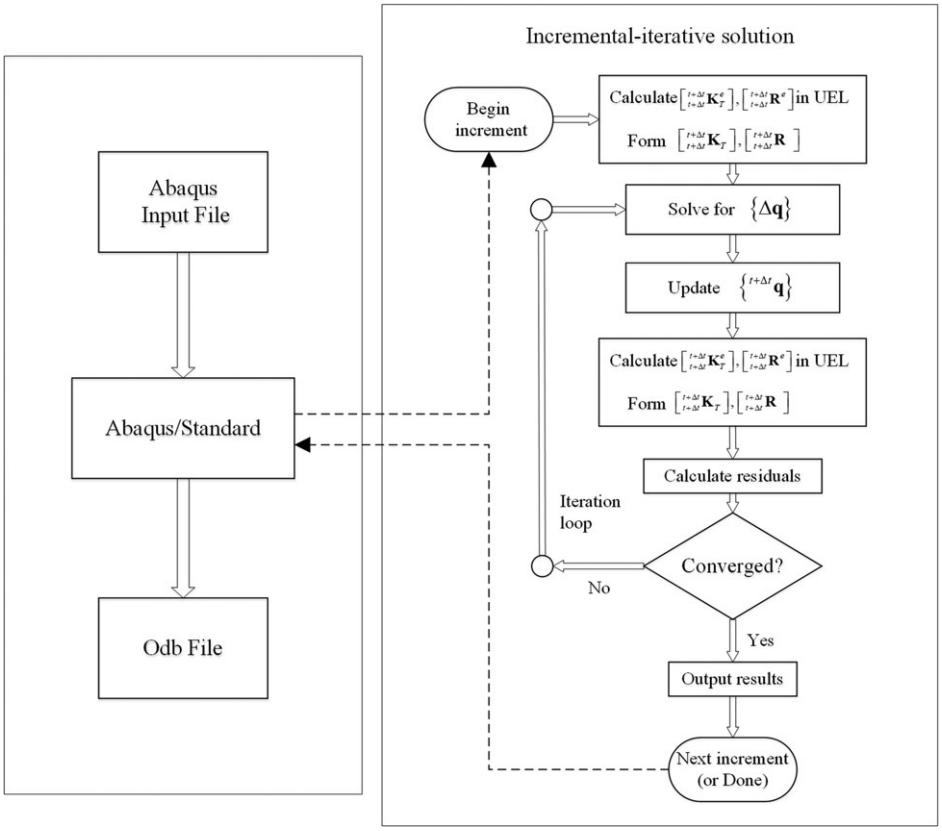

FIGURE 3 The incremental-iterative Newton-Raphson scheme in Abaqus/Standard. UEL, user element

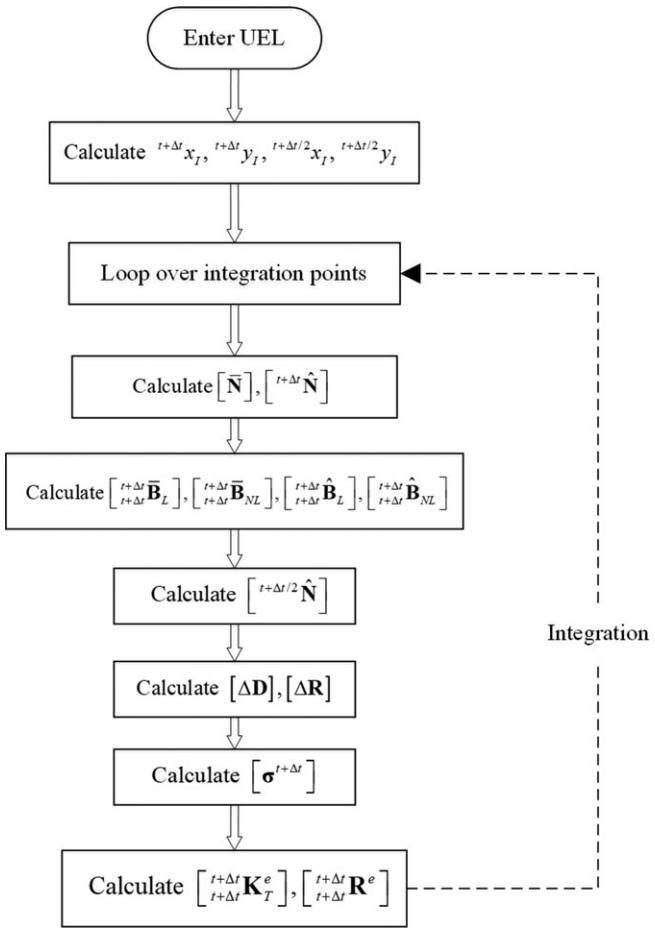

FIGURE 4 The computation flowchart of the nonlinear formulations of element US-ATFQ4. UEL, user element

where $E' = E$ and $\mu' = \mu$ for plane stress problem, whereas $E' = E/(1-\mu^2)$ and $\mu' = \mu/(1-\mu)$ for plane strain problem, in which E and μ are Young's modulus and Poisson's ratio, respectively; and $\Delta D_{\alpha\beta}$, which are also defined at the midpoint of the time interval, are the strain increments, ie,

$$\Delta D_{\alpha\beta} = \frac{1}{2}\left({}_{t+\Delta t/2}u_{\alpha,\beta} + {}_{t+\Delta t/2}u_{\beta,\alpha}\right), \quad (\alpha,\beta = 1,2). \tag{36}$$

3.2 | Numerical implementation

In this paper, the present geometric nonlinear formulations of element US-ATFQ4 will be compiled and implemented in commercial software SIMULA Abaqus via the UEL subroutine,[5] and the corresponding flowchart is given by Figure 3. First, an input-file is written with Abaqus keywords[5] to define an analysis. Then, this input-file is submitted to Abaqus/Standard and the program is run to solve specified problems. All results will be output by automatically writing in an Odb file. Figure 3 also shows the incremental-iterative Newton-Raphson schemes for solving the nonlinear problems.

All terms of the element formulations are evaluated by using a 2×2 Gauss integration scheme. Figure 4 plots the computation flowchart of the nonlinear formulations of element US-ATFQ4 in UEL.

4 | NUMERICAL EXAMPLES

In this section, 4 examples using traditional regular and new distorted mesh divisions are adopted to assess the performance of the new formulations. All nonlinear finite element equations are solved by the full Newton-Raphson method and automatic incrementation control scheme (the size of time increments is automatically adjusted according to convergence) embedded in Abaqus.[5] The initial size of time increment is set to 0.1 (the total time is 1) because of the highly

geometric nonlinearity. The results obtained by some other plane quadrilateral models, as listed in the following, are also given for comparison.

Plane quadrilateral element models for geometrically nonlinear analysis:

- CPS4/CPE4 (Q4): the 4-node isoparametric elements in Abaqus, with full 2×2 integration scheme, and for plane stress and strain states, respectively.[5]
- CPS4R/CPE4R: the 4-node isoparametric elements in Abaqus, with reduced 1 × 1 integration scheme and enhanced hourglass control approach, and for plane stress and strain states, respectively.[5]
- CPS4I/CPE4I: the 4-node nonconforming isoparametric elements in Abaqus, with enhanced assumed strain, and for plane stress and strain states, respectively.[5]

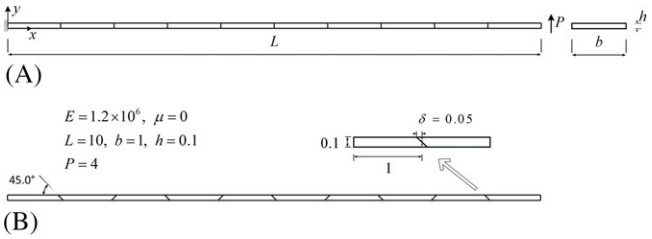

FIGURE 5 A slender cantilever beam subjected to end resultant shear force and 2 mesh cases. A, Regular mesh; B, Distorted mesh

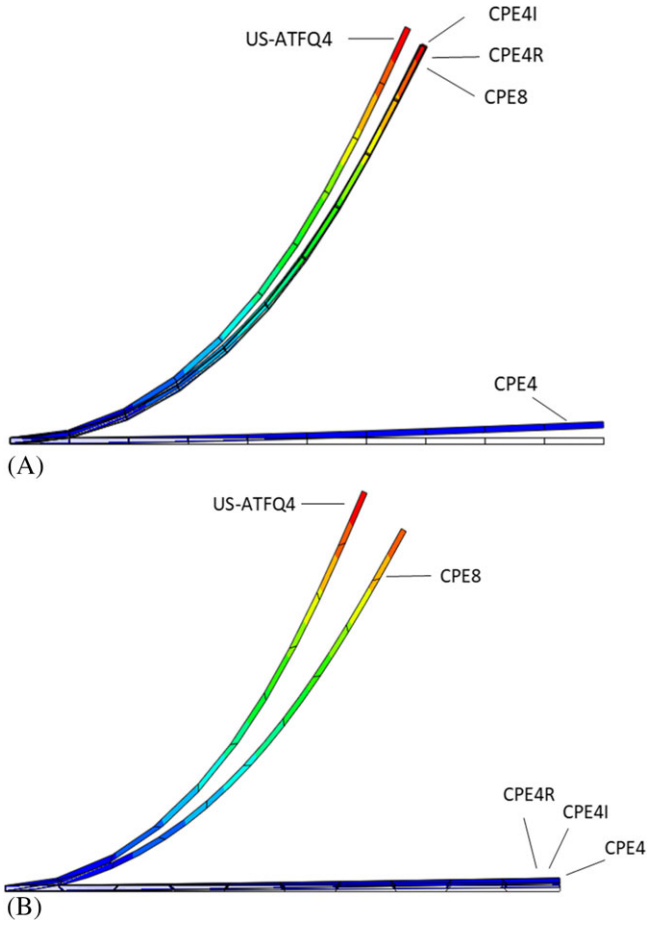

FIGURE 6 The deformed shapes of slender cantilever beam subjected to end resultant shear force. A, Results obtained by 1 × 10 regular rectangle elements; B, Results obtained by 1 × 10 distorted elements [Colour figure can be viewed at wileyonlinelibrary.com]

- CPS8/CPE8: the 8-node isoparametric elements in Abaqus, with full 3×3 integration scheme, and for plane stress and strain states, respectively.[5]
- HW14-S: the mixed 4-node Hu-Washizu element based on skew coordinates proposed by Wisniewski and Turska.[39]
- HW18-SS: the mixed/enhanced 4-node Hu-Washizu element based on skew coordinates proposed by Wisniewski and Turska.[39]
- PFR4: the 4-node plane quadrilateral element with rotational DOF proposed by Zouari et al.[41]
- PFR4I: the 4-node nonconforming plane quadrilateral element with rotational DOF proposed by Zouari et al.[41]
- QM6: the nonlinear 4-node nonconforming plane quadrilateral element proposed by Battini,[47] which was extended from the linear element QM6 proposed by Taylor et al.[4]
- Qnew: the nonlinear 4-node plane quadrilateral element proposed by Battini,[47] which was extended from the linear element proposed by Fredriksson and Ottosen.[48]

4.1 | Cantilever beam subjected to end shear force

As shown in Figure 5, a slender elastic cantilever beam is subjected to a resultant shear force P at its free end. The reference results of the tip vertical and horizontal displacements have been reported by Sze et al.[49] Two mesh cases, 1×10 elements with regular rectangle and distorted (isosceles trapezoid) shapes, are considered. The material (Young's modulus E and Poisson's ratio μ) and the geometry parameters are also given in Figure 5.

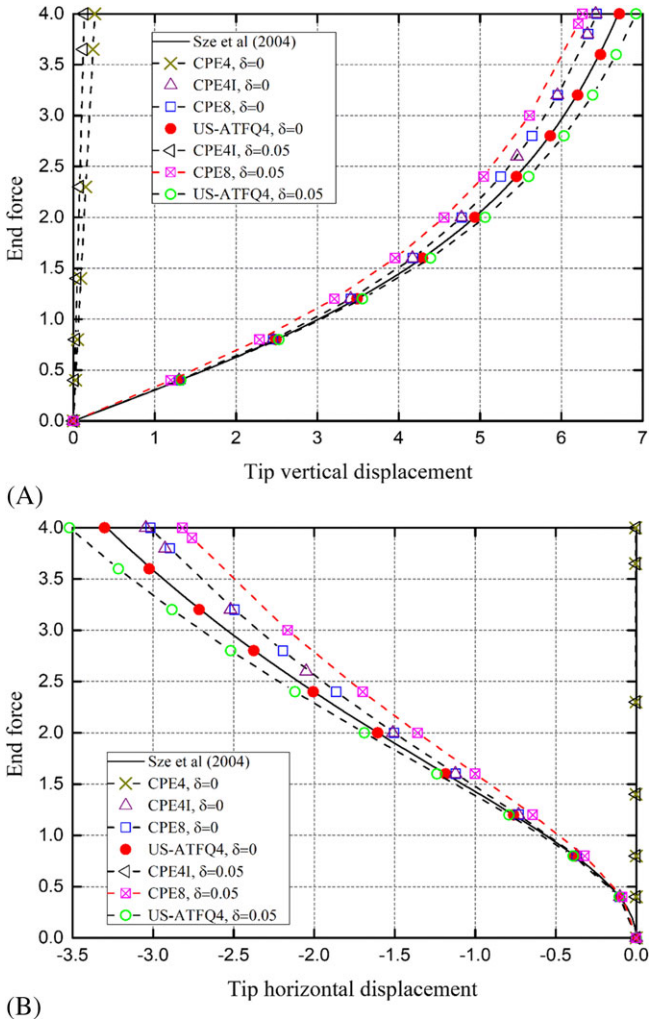

FIGURE 7 Load-displacement curves for a slender cantilever beam subjected to an end resultant shear force with $\mu = 0$ (Example 4.1). A, End shear force versus vertical displacement curves, 1×10 regular and distorted mesh; B, End shear force versus horizontal displacement curves, 1×10 regular and distorted mesh [Colour figure can be viewed at wileyonlinelibrary.com]

Figure 6 plots the deformed shapes obtained by elements US-ATFQ4, CPE4, CPE4I, CPE4R, and CPE8. Moreover, the resulting load-displacement curves of US-ATFQ4 compared with CPE4, CPE4I, and CPE8 are given in Figure 7. Table 1 lists the total number of increments NINC and iterations NITER required for obtaining the converged ultimate solutions using 2 mesh cases. As described in the beginning of Section 4, during the whole computation process, the time increment is automatically adjusted according to the convergence. Here, a fixed time increment case is also tested. Table 2 gives the results of the vertical and horizontal tip displacements obtained by a fixed time increment size 0.1 (ie, NINC = 10).

TABLE 1 The number of increments NINC and iterations NITER required to obtain the converged ultimate solutions for the slender cantilever beam subjected to an end resultant shear force problem (Figure 5)

(a) 1 × 10 regular mesh					
Mesh (a)	**CPE4**	**CPE4I**	**CPE4R**	**CPE8**	**US-ATFQ4**
NINC	6	9	11	10	10
NITER	7	43	52	51	50
(b) 1 × 10 distorted mesh					
Mesh (b)	**CPE4**	**CPE4I**	**CPE4R**	**CPE8**	**US-ATFQ4**
NINC	6	6	6	9	10
NITER	7	7	7	42	55

TABLE 2 Results of vertical and horizontal tip displacements for the slender cantilever beam subjected to an end resultant shear force (Figure 5), fixed time increment 0.1

(a) 1 × 10 regular mesh								
Mesh (a)			**V_{Tip}**				**U_{Tip}**	
Total time	**CPE4I**	**CPE8**	**US-ATFQ4**	**Sze et al[49]**	**CPE4I**	**CPE8**	**US-ATFQ4**	**Sze et al[49]**
0.0	0.0000	0.0000	**0.0000**	0.0000	0.0000	0.0000	**0.0000**	0.0000
0.1	1.2985	1.2976	**1.3069**	1.3086	−0.1018	−0.1016	**−0.1029**	−0.1033
0.2	2.4558	2.4562	**2.4907**	2.4926	−0.3704	−0.3701	**−0.3799**	−0.3808
0.3	3.4101	3.4132	**3.4874**	3.4879	−0.7316	−0.7308	**−0.7616**	−0.7626
0.4	4.1701	4.1755	**4.2937**	4.2919	−1.1234	−1.1208	**−1.1838**	−1.1840
0.5	4.7732	4.7778	**4.9371**	4.9325	−1.5113	−1.5038	**−1.6055**	−1.6040
0.6	5.2517	5.2567	**5.4507**	5.4436	−1.8759	−1.8633	**−2.0054**	−2.0020
0.7	5.6361	5.6422	**5.8646**	5.8550	−2.2117	−2.1937	**−2.3753**	−2.3696
0.8	5.9490	5.9570	**6.2016**	6.1903	−2.5176	−2.4947	**−2.7128**	−2.7050
0.9	6.2071	6.2175	**6.4829**	6.4670	−2.7952	−2.7680	**−3.0232**	−3.0098
1.0	6.4227	6.4362	**6.7146**	6.6984	−3.0471	−3.0162	**−3.3005**	−3.2863
(b) 1 × 10 distorted mesh								
Mesh (b)			**V_{Tip}**				**U_{Tip}**	
Total time	**CPE4I**	**CPE8**	**US-ATFQ4**	**Sze et al[49]**	**CPE4I**	**CPE8**	**US-ATFQ4**	**Sze et al[49]**
0.0	0.0000	0.0000	**0.0000**	0.0000	0.0000	0.0000	**0.0000**	0.0000
0.1	0.0136	1.1990	**1.3198**	1.3086	0.0000	−0.0868	**−0.1048**	−0.1033
0.2	0.0272	2.2886	**2.5279**	2.4926	0.0000	−0.3206	**−0.3906**	−0.3808
0.3	0.0407	3.2091	**3.5556**	3.4879	−0.0001	−0.6428	**−0.7902**	−0.7626
0.4	0.0541	3.9579	**4.3932**	4.2919	−0.0002	−0.9996	**−1.2376**	−1.1840
0.5	0.0675	4.5597	**5.0643**	4.9325	−0.0002	−1.3571	**−1.6883**	−1.6040
0.6	0.0808	5.0448	**5.6010**	5.4436	−0.0003	−1.6979	**−2.1182**	−2.0020
0.7	0.0941	5.4393	**6.0338**	5.8550	−0.0005	−2.0151	**−2.5176**	−2.3696
0.8	0.1073	5.7640	**6.3855**	6.1903	−0.0006	−2.3069	**−2.8821**	−2.7050
0.9	0.1204	6.0303	**6.6761**	6.4670	−0.0007	−2.5691	**−3.2144**	−3.0098
1.0	0.1335	6.2617	**6.9209**	6.6984	−0.0009	−2.8169	**−3.5190**	−3.2863

For the regular mesh (distortion parameter $\delta = 0$), it can be observed that the results of the present element US-ATFQ4 agree very well with the reference curves. Element US-ATFQ4 is found to be more accurate than the Abaqus nonconforming model CPE4I and CPE4R, whereas CPE4 shows a very poor precision. For distorted mesh ($\delta = 0.05$), the proposed element US-ATFQ4 still keeps high accuracy. However, element CPE4I and CPE4R only provide very poor results similar to those obtained by CPE4. Furthermore, although the DOF of element US-ATFQ4 are much fewer than those of 8-node element CPE8, the results obtained by US-ATFQ4 are found to be better than those given by CPE8 for both 2 mesh cases. From Table 2, it can be seen that the proposed element US-ATFQ4 can also produce excellent results when the fixed time increment 0.1 is used.

Besides, this example is redone with a nonzero Poisson's ratio, ie, $\mu = 0.3$, under plane stress conditions. The reference results of the tip vertical and horizontal displacements are obtained by using CPS8 with a fine mesh (2×200 rectangular elements). The resulting load-displacement curves of US-ATFQ4 compared with CPS4, CPS4I, and CPS8 are given in Figure 8. The same conclusions as discussed earlier can be drawn.

Another similar example proposed by Wisniewski and Turska[39] is also taken into consideration. The only differences come from material and geometry parameters, ie, $E = 10^6$, $\mu = 0.3$, $L = 100$, $b = 1$, $h = 1$, and the resultant shear force $P = 200$. The final rotation of this cantilever's tip is close to 90°. The reference results of the tip vertical and horizontal displacements are also obtained by using CPS8 with a fine mesh (2×200 rectangular elements). The resulting load-displacement curves of US-ATFQ4 (with 1×20 rectangular elements) compared with HW14-S and HW18-SS (both with 1×100 rectangular elements) are given in Figure 9. It can be seen that the proposed element US-ATFQ4 can produce excellent results with coarse mesh.

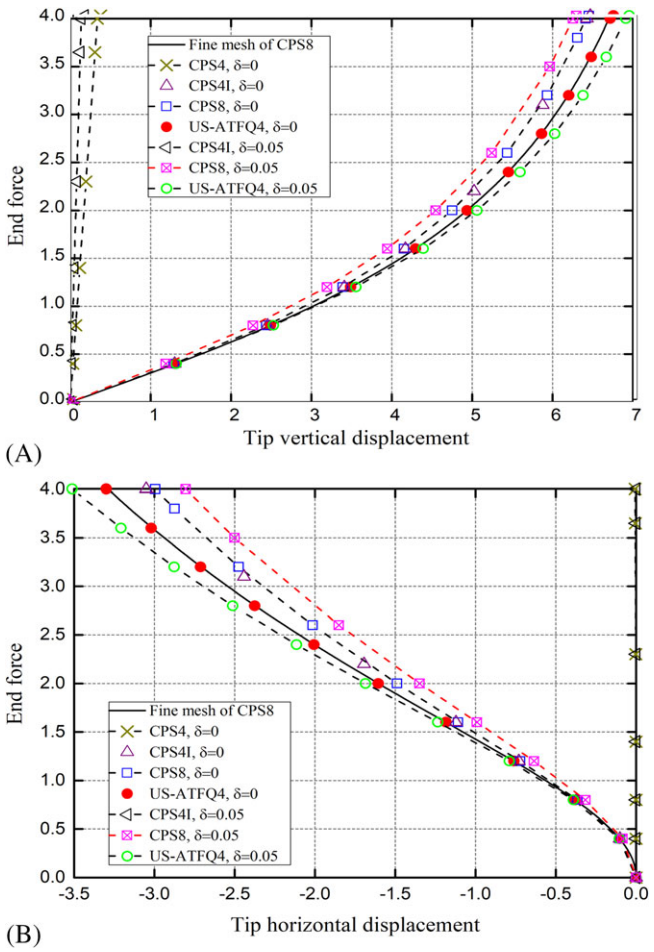

FIGURE 8 Load-displacement curves for a slender cantilever beam subjected to an end resultant shear force with $\mu = 0.3$ (Example 4.1). A, End shear force versus vertical displacement curves, 1×10 regular and distorted mesh; B, End shear force versus horizontal displacement curves, 1×10 regular and distorted mesh [Colour figure can be viewed at wileyonlinelibrary.com]

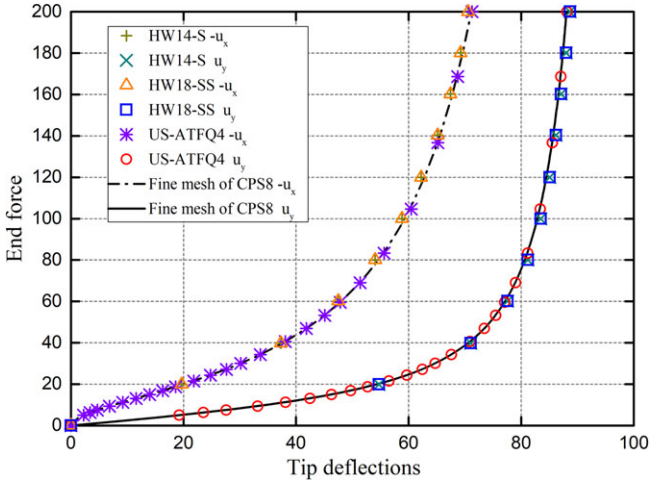

FIGURE 9 Load-displacement curves for a slender cantilever beam subjected to an end resultant shear force[39] [Colour figure can be viewed at wileyonlinelibrary.com]

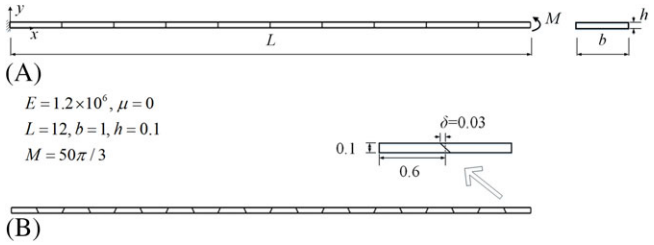

FIGURE 10 A slender cantilever beam subjected to end moment and 2 mesh cases. A, Regular mesh; B, Distorted mesh

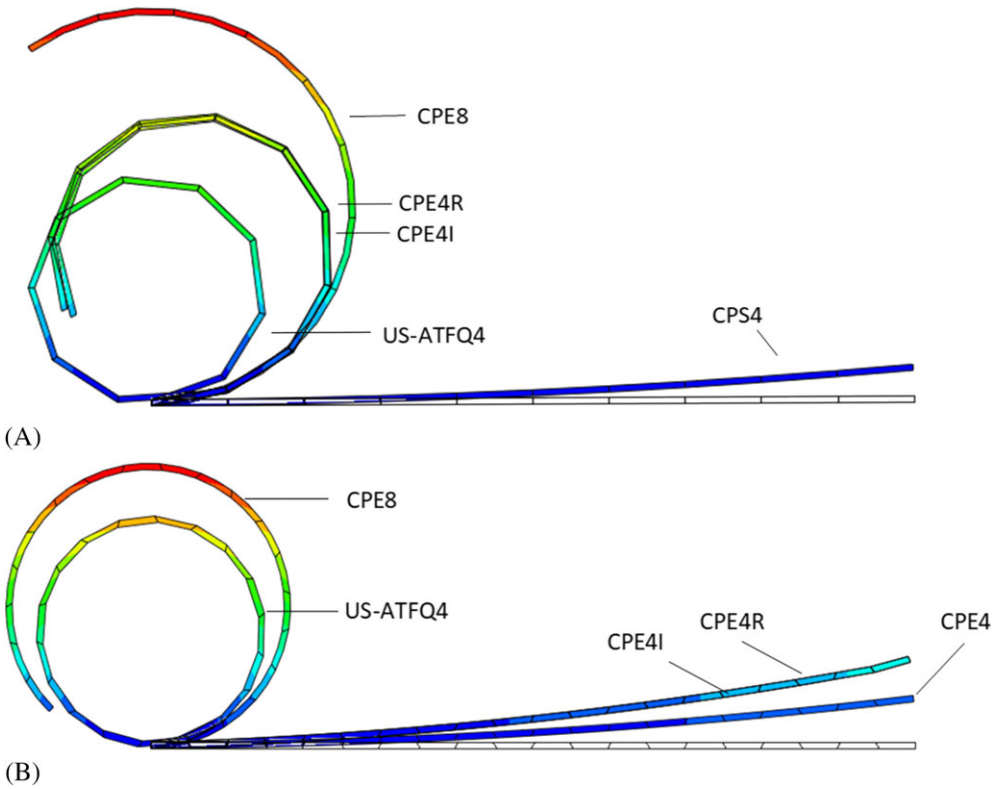

FIGURE 11 The deformed shapes of slender cantilever beam subjected to end resultant moment. A, Results obtained by regular mesh; B, Results obtained by distorted mesh [Colour figure can be viewed at wileyonlinelibrary.com]

4.2 | Cantilever beam subjected to end moment

As shown in Figure 10, a slender cantilever beam is subjected to a resultant moment M at its free end. All material and geometry parameters are also given in Figure 10. The analytical solution for this problem is $R = EI/M$,[49] where I is the section moment of inertia and R is the radius of a circular that the cantilever beam forms. Hence, when the end resultant moment M is taken to be $2\pi EI/L$, the cantilever beam will bend to be a circle. The analytical solutions of the end moment against tip deflections have been given in the work of Sze et al.[49]

Two mesh cases, 1×10 regular rectangle elements and distorted (isosceles trapezoid) elements, are considered. The deformed shapes obtained by US-ATFQ4, CPE4, CPE4I, CPE4R, and CPE8 are plotted in Figure 11. In addition, the load-displacement curves of US-ATFQ4 compared with CPE4, CPE4I, and CPE8 are shown in Figure 12. Table 3 lists the total number of increments NINC and iterations NITER required for obtaining the converged ultimate solutions. Furthermore, Table 4 lists the vertical and horizontal tip displacements obtained by a fixed time increment 0.01 (ie, NINC = 100).

For the regular mesh with 1×10 rectangular elements ($\delta = 0$), elements CPE4, CPE4I, CPE4R, and even CPE8 cannot provide good results. On the contrary, under the same mesh, the results obtained by the present element US-ATFQ4 exhibit high accuracy. For the mesh with 1×20 distorted elements ($\delta = 0.03$), the results of CPE4I and CPE4R are much worse than those obtained by using the 1×10 regular mesh. However, it can be seen that the solutions of US-ATFQ4 can still keep high accuracy. Similar to the previous example, although the DOF of CPE8 are much more than those of US-ATFQ4, US-ATFQ4 still performs better than CPE8 under both regular and distorted meshes.

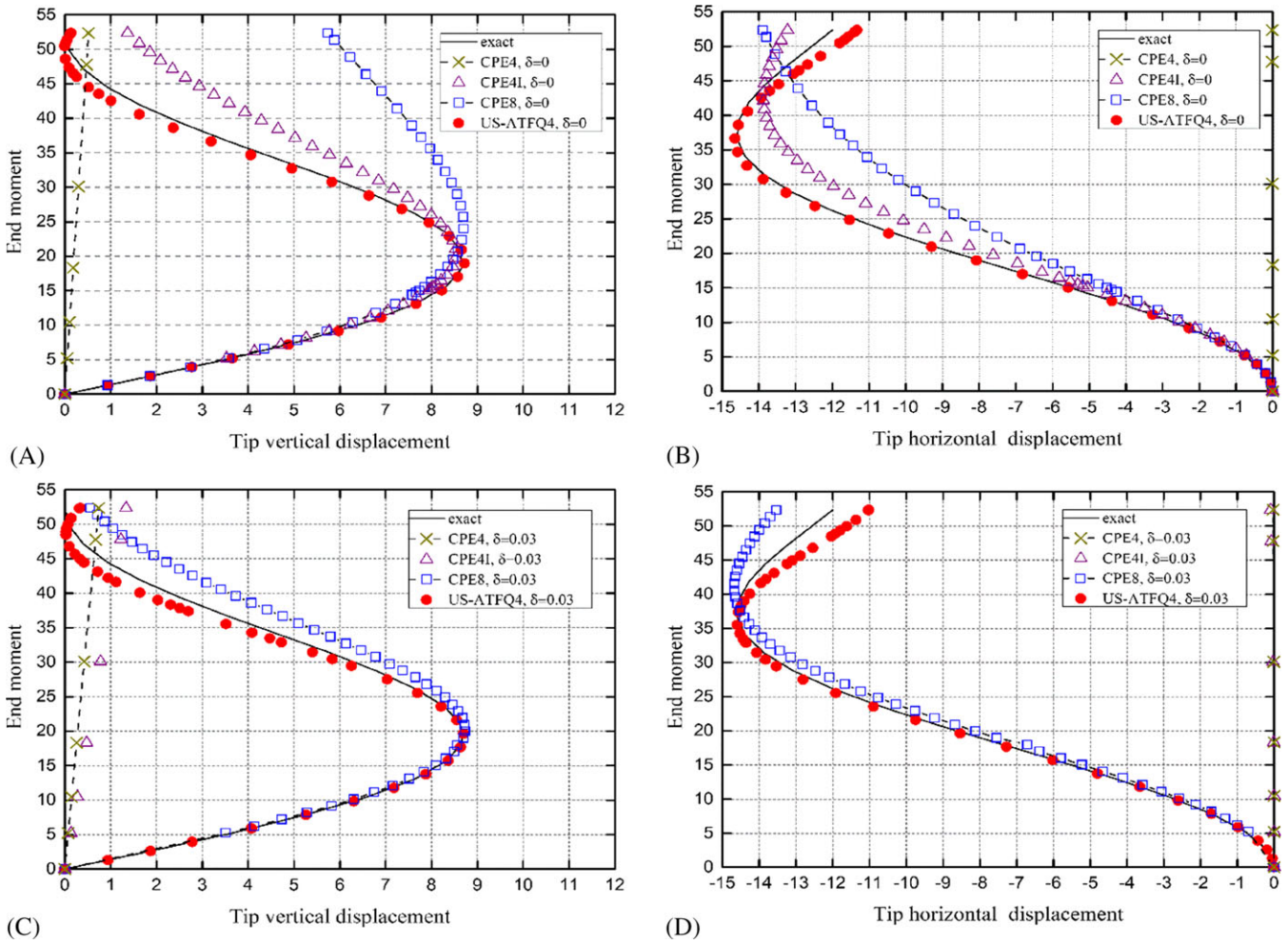

FIGURE 12 Load-displacement curves for a slender cantilever beam subjected to an end resultant moment with $\mu = 0$ (Example 4.2). A, End moment versus vertical displacement curves, 1×10 regular mesh; B, End moment versus horizontal displacement curves, 1×10 regular mesh; C, End moment versus vertical displacement curves, 1×20 distorted mesh; D, End moment versus horizontal displacement curves, 1×20 distorted mesh [Colour figure can be viewed at wileyonlinelibrary.com]

TABLE 3 The number of increments NINC and iterations NITER required to obtain the converged ultimate solutions for the slender cantilever beam subjected to an end resultant moment (Figure 10)

(a) 1 × 10 regular mesh					
Mesh (a)	**CPE4**	**CPE4I**	**CPE4R**	**CPE8**	**US-ATFQ4**
NINC	6	44	39	36	34
NITER	8	264	222	220	203
(b) 1 × 20 distorted mesh					
Mesh (b)	**CPE4**	**CPE4I**	**CPE4R**	**CPE8**	**US-ATFQ4**
NINC	6	6	6	49	41
NITER	8	13	12	313	223

TABLE 4 Vertical and horizontal tip displacements for the slender cantilever beam subjected to an end resultant moment (Figure 10), fixed time increment 0.01

(a) 1 × 10 regular mesh								
Mesh (a)			V_{Tip}				U_{Tip}	
Total time	**CPE4I**	**CPE8**	**US-ATFQ4**	**Sze et al[49]**	**CPE4I**	**CPE8**	**US-ATFQ4**	**Sze et al[49]**
0.0	0.0000	0.0000	**0.0000**	0.0000	0.0000	0.0000	**0.0000**	0.0000
0.1	3.6124	3.5855	**3.6499**	3.6480	−0.7599	−0.7466	**−0.7730**	−0.7740
0.2	6.4381	6.2884	**6.6136**	6.5980	−2.7802	−2.5894	**−2.9235**	−2.9180
0.3	8.0804	7.8849	**8.3626**	8.3330	−5.5003	−4.8229	**−5.9843**	−5.9450
0.4	8.4920	8.5854	**8.6499**	8.6370	−8.3130	−6.9802	**−9.2977**	−9.1940
0.5	7.8923	8.6725	**7.5698**	7.6390	−10.7363	−8.8636	**−12.1711**	−12.0000
0.6	6.6380	8.3712	**5.5375**	5.7580	−12.4912	−10.4223	**−14.0474**	−13.8710
0.7	5.1014	7.8383	**3.1869**	3.5710	−13.5012	−11.6679	**−14.6504**	−14.5950
0.8	3.5882	7.1785	**1.2019**	1.6500	−13.8405	−12.6349	**−14.0673**	−14.2700
0.9	2.3019	6.4606	**0.1167**	0.4050	−13.6666	−13.3628	**−12.7371**	−13.2470
1.0	1.3454	5.7298	**0.1346**	0.0000	−13.1618	−13.8897	**−11.3299**	−12.0000
(b) 1 × 20 distorted mesh								
Mesh (b)			V_{Tip}				U_{Tip}	
Total time	**CPE4I**	**CPE8**	**US-ATFQ4**	**Sze et al[49]**	**CPE4I**	**CPE8**	**US-ATFQ4**	**Sze et al[49]**
0.0	0.0000	0.0000	**0.0000**	0.0000	0.0000	0.0000	**0.0000**	0.0000
0.1	0.1379	3.6050	**3.6518**	3.6480	−0.0010	−0.7549	**−0.7754**	−0.7740
0.2	0.2746	6.5185	**6.6171**	6.5980	−0.0038	−2.8274	**−2.9349**	−2.9180
0.3	0.4101	8.2617	**8.3607**	8.3330	−0.0086	−5.7143	**−6.0119**	−5.9450
0.4	0.5447	8.6870	**8.6274**	8.6370	−0.0151	−8.7768	**−9.3436**	−9.1940
0.5	0.6784	7.9684	**7.5067**	7.6390	−0.0236	−11.4502	**−12.2242**	−12.0000
0.6	0.8113	6.4825	**5.4198**	5.7580	−0.0338	−13.3680	**−14.0777**	−13.8710
0.7	0.9437	4.6721	**3.0234**	3.5710	−0.0460	−14.3997	**−14.6113**	−14.5950
0.8	1.0751	2.9233	**1.0432**	1.6500	−0.0600	−14.6201	**−13.9134**	−14.2700
0.9	1.2064	1.5037	**0.0618**	0.4050	−0.0759	−14.2284	**−12.4629**	−13.2470
0.9	1.2064	1.5037	**0.0618**	0.4050	−0.0759	−14.2284	**−12.4629**	−13.2470
1.0	1.3367	0.5466	**0.3028**	0.0000	−0.0937	−13.4710	**−11.0282**	−12.0000

Besides, this example is redone with a nonzero Poisson's ratio, ie, $\mu = 0.3$, under plane stress conditions. The reference results of the tip vertical and horizontal displacements are obtained by using CPS8 with a fine mesh (2×200 rectangular elements). The resulting load-displacement curves of US-ATFQ4 compared with CPS4, CPS4I, and CPS8 are given in Figure 13. The same conclusions as discussed earlier can be drawn.

4.3 | Angle frame

As shown in Figure 14, an angle frame structure, which is assumed to be under plane stress state, is clamped at the left end and subjected to a uniformly distributed horizontal force F at the right end. The material and geometry parameters

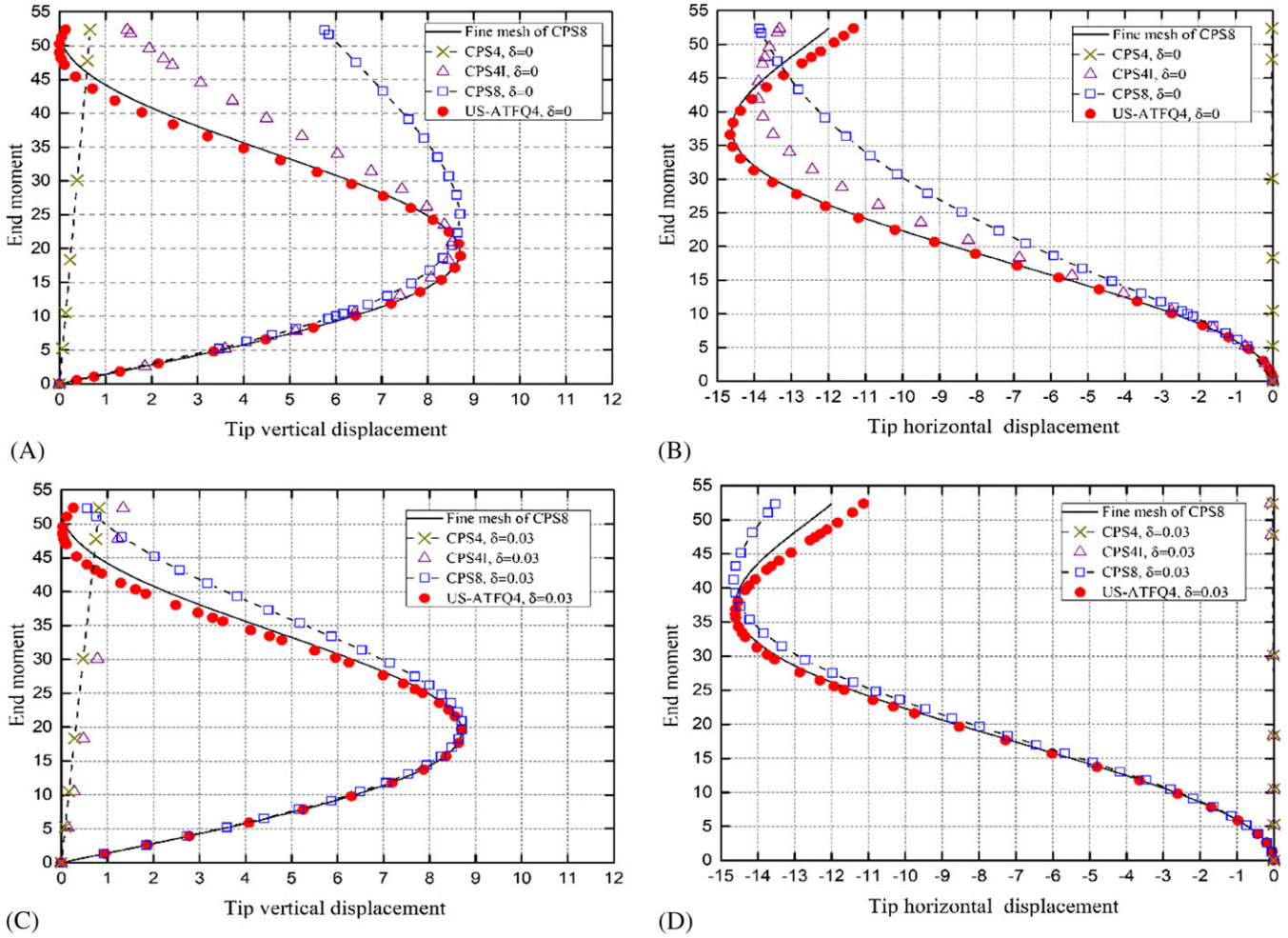

FIGURE 13 Load-displacement curves for a slender cantilever beam subjected to an end resultant moment with $\mu = 0.3$ (Example 4.2). A, End moment versus vertical displacement curves, 1×10 regular mesh; B, End moment versus horizontal displacement curves, 1×10 regular mesh; C, End moment versus vertical displacement curves, 1×20 distorted mesh; D, End moment versus horizontal displacement curves, 1×20 distorted mesh [Colour figure can be viewed at wileyonlinelibrary.com]

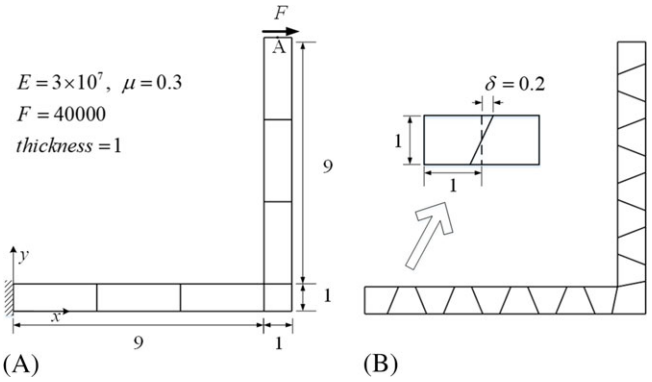

FIGURE 14 An angle frame structure and 2 mesh cases. A, Regular mesh with 7 rectangular elements; B, Distorted mesh with 19 elements

are also given in Figure 14. The reference results are obtained by using CPS8 with a fine mesh (304 rectangular elements). Two mesh cases, (i) regular mesh with 7 rectangular elements suggested by Zouari et al[41] and (ii) distorted mesh with 19 distorted (isosceles trapezoid) elements suggested by Battini,[47] are considered. The deformed shape obtained by US-ATFQ4, CPS4, and CPS4I compared with the reference deformed configuration are plotted in Figure 15. Furthermore, the load-displacement curves of US-ATFQ4 compared with CPS4, CPS4I, PFR4,[41] PFR4I,[41] QM6,[47] and Qnew[47] obtained

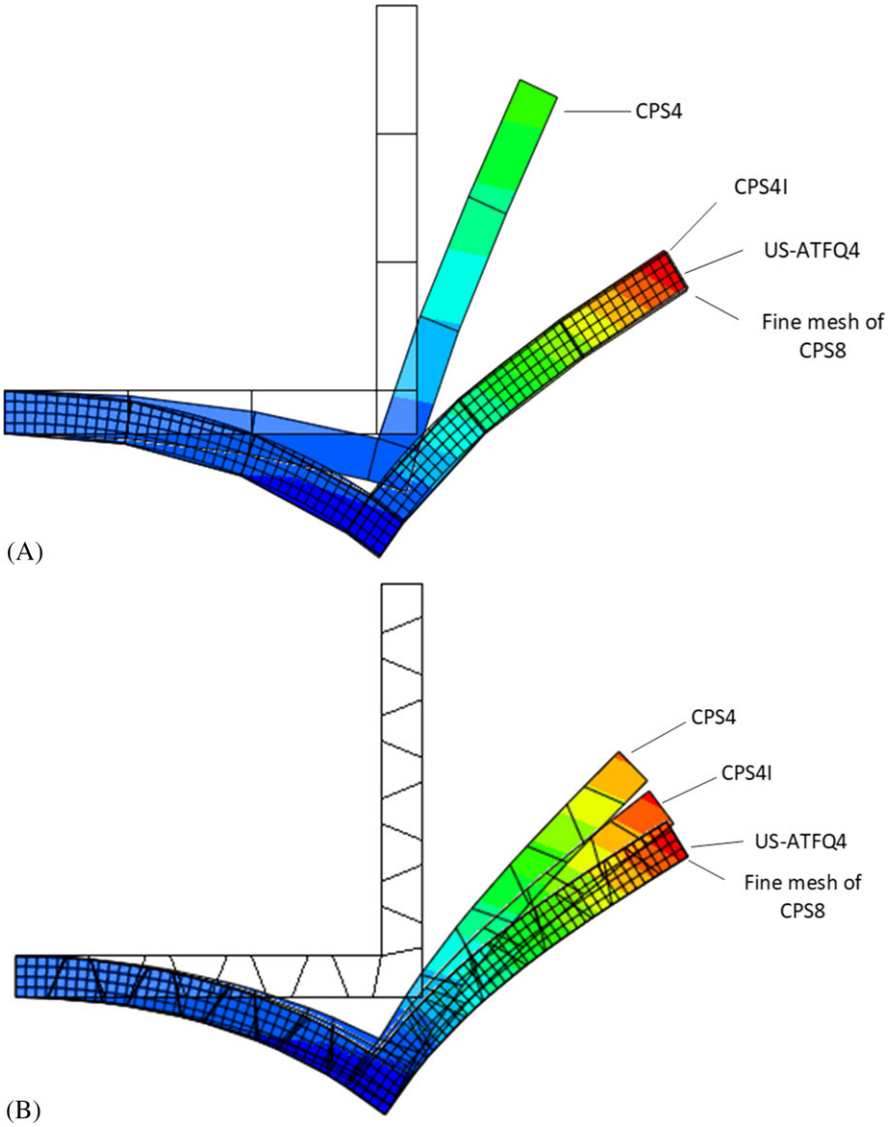

FIGURE 15 The deformed shapes of the angle frame structure. A, Results obtained by regular mesh with 7 rectangular elements; B, Results obtained by mesh with 19 distorted elements [Colour figure can be viewed at wileyonlinelibrary.com]

by 2 meshes are shown in Figure 16. Table 5 lists the total number of increments NINC and iterations NITER required for obtaining the converged ultimate solutions.

For the regular mesh, elements US-ATFQ4, PFR4I, and CPS4I all can agree well with the reference configuration obtained by CPS8 with fine mesh. In addition, for the distorted mesh, US-ATFQ4 can still keep high accuracy, whereas CPS4I, QM6, and Qnew lose their precision greatly.

4.4 | Lee's frame buckling problem

Lee's frame buckling problem is one of the National Agency for Finite Element Methods and Standards proposed benchmarks.[50] As shown in Figure 17, 2 mesh cases with 25 regular rectangle elements and 25 distorted (isosceles trapezoid) elements are considered. In order to study the postbucking nonlinear behavior of the frame at point A, the modified Riks method[5,45] is employed here. In such Riks method, the load magnitude is taken as an additional unknown and the loads and the displacements are solved simultaneously. Unlike the normal incremental-iterative solution strategy under load control, the Riks method augments the n-dimensional space of unknown displacements to an $(n + 1)$-dimensional space of unknowns. Therefore, another quantity, ie, arc length l, must be used to measure the progress of solution along the static equilibrium path in load-displacement space, ie, a path-following constraint should be added. More details about the Riks method were explained in the work of de Borst et al.[45]

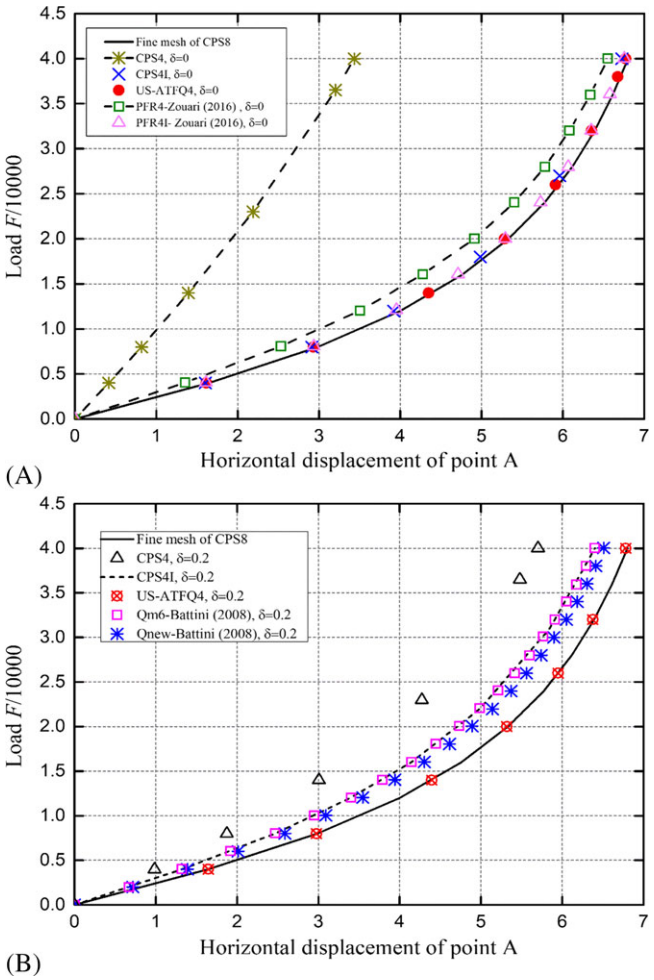

FIGURE 16 Load versus horizontal displacement curves for the angle frame problem (Example 4.3). A, 7 regular rectangle elements; B, 19 distorted elements [Colour figure can be viewed at wileyonlinelibrary.com]

TABLE 5 The number of increments NINC and iterations NITER required to obtain the converged ultimate solutions for the angle frame problem (Figure 14)

(a) Regular mesh with 7 rectangular elements			
Mesh (a)	**CPS4**	**CPS4I**	**US-ATFQ4**
NINC	6	6	8
NITER	12	26	31
(b) Distorted mesh with 19 distorted elements			
Mesh (b)	**CPS4**	**CPS4I**	**US-ATFQ4**
NINC	6	7	7
NITER	18	27	27

Similar to previous examples, the automatic incrementation control scheme is chosen, and the initial increment size in arc length along the static equilibrium path Δl_{in}, the maximum arc length increment $\Delta l_{\max}$, and the maximum value of the load proportionality factor λ_{end} are set to 0.1, 1, and 30, respectively. The reference results are obtained by using a fine mesh containing 60 B22 elements (B22 is the 3-node quadratic beam element of Abaqus[5]). The load-displacement curves of US-ATFQ4 compared with CPS4 and CPS4I are plotted in Figure 18.

Similar to the previous examples, the results obtained by CPS4I agree well with the reference solutions only for the regular mesh. However, the present element US-ATFQ4 performs very well for both regular and distorted meshes. Therefore, it is clear that the present new formulations also exhibit excellent performance in predicting the snapback instability of

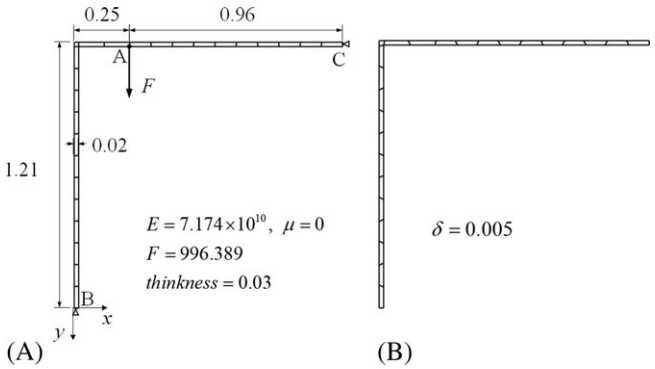

FIGURE 17 A Lee's frame structure and 2 mesh divisions

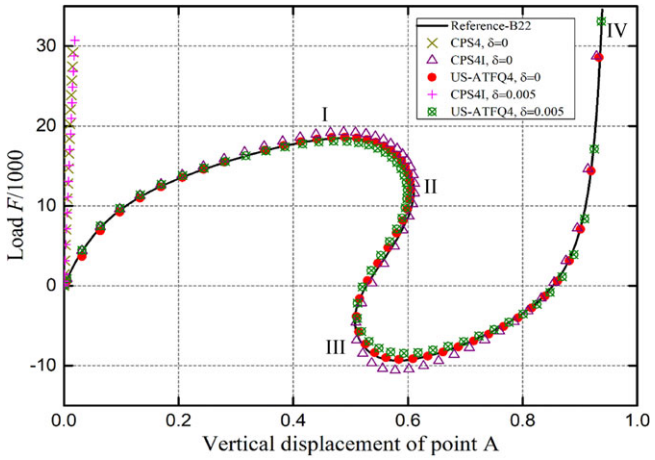

FIGURE 18 Load versus vertical displacement curves for the Lee's frame buckling problem with $\mu = 0$ (Example 4.4) [Colour figure can be viewed at wileyonlinelibrary.com]

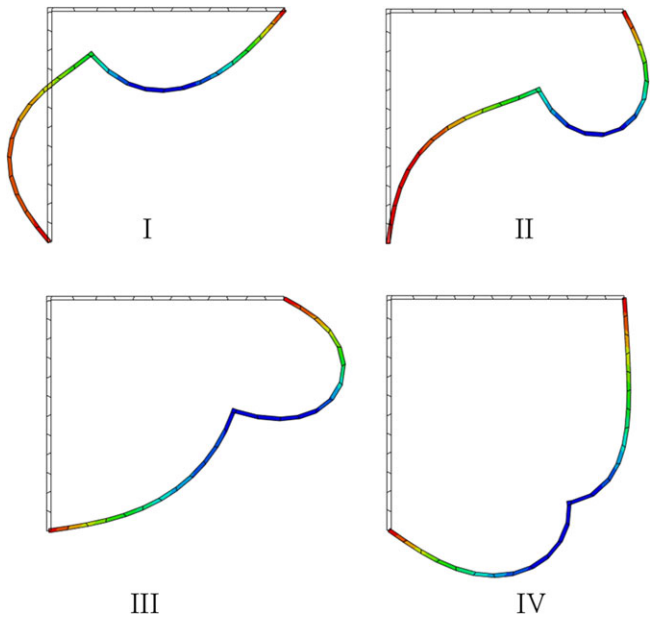

FIGURE 19 Four deformed states (states I, II, III, and IV are given in Figure 18) of Lee's frame structure obtained by 25 distorted US-ATFQ4 elements [Colour figure can be viewed at wileyonlinelibrary.com]

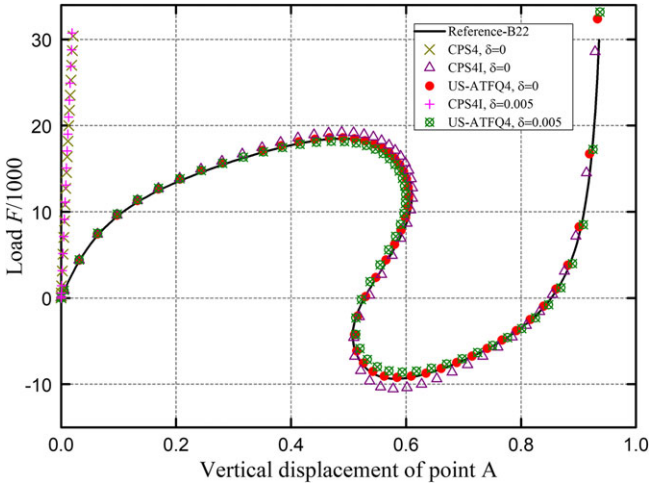

FIGURE 20 Load versus vertical displacement curves for Lee's frame buckling problem with $\mu = 0.3$ (Example 4.4) [Colour figure can be viewed at wileyonlinelibrary.com]

Lee's frame by employing the modified Riks method. Four deformed states of the frame corresponding to states I, II, III, and IV in Figure 18 obtained by US-ATFQ4 with 25 distorted elements are shown in Figure 19.

Besides, this example is redone with a nonzero Poisson's ratio, ie, $\mu = 0.3$. The resulting load-displacement curves of US-ATFQ4 compared with CPS4 and CPS4I are given in Figure 20. The situation is the same as that with zero Poisson's ratio.

5 | CONCLUDING REMARKS

An approach to develop a 4-node, 8-DOF plane quadrilateral finite element model with high-precision and high-distortion tolerance, for both linear and nonlinear problems, has been attracting many researchers for a long time. Unfortunately, because of some inherent defects, it is almost an impossible mission just like the contradiction defined by MacNeal's theorem.[28,29]

Recently, a breakthrough was achieved for linear elastic problems. A series of 2D and 3D unsymmetric finite element models with analytical trial functions were successfully constructed.[30,51,52] These elements contain the analytical solutions for homogeneous control equations of linear elasticity and exhibit excellent precision for both regular and severely distorted meshes. Especially, the 4-node, 8-DOF plane quadrilateral element US-ATFQ4[30] and the 8-node, 24-DOF 3D hexahedral element US-ATFH8[52] can completely break through the limitation given by MacNeal's theorem. However, it should be noted that these successes must depend on the general solutions of linear elasticity. Once there are no such solutions, for example, nonlinear problems, could anyone find an effective way to keep the same performance? Therefore, how to modify original formulations into incremental forms for nonlinear applications and design an appropriate updated algorithm become the key of the whole job.

In this paper, the unsymmetric 4-node, 8-DOF plane element US-ATFQ4[30] is extended to geometric nonlinear analysis. First, the analytical trial functions should be updated at each iterative step in the framework of the UL formulation that takes the current configuration, ie, the configurations at the beginning of an incremental step, as the reference configuration during that step. Second, an appropriate stress update algorithm in which the Cauchy stresses is updated by the Hughes-Winget method[34] is adopted to estimate the current stress field. Numerical examples show that the new nonlinear element US-ATFQ4 also possesses amazing performance for geometric nonlinear analysis, no matter whether regular or distorted meshes are used. It again demonstrates the advantages of the unsymmetric finite element method with analytical trial functions, although these functions only come from linear elasticity.

This is the first attempt to generalize the finite element model with the analytical trial functions of linear elasticity to nonlinear application, and only the small strain with large displacement/rotation problems are concerned. Since a rate form of updating algorithm is adopted, the formulations can be straightforward extended to large deformation problems. This topic will be discussed in another paper in the near future.

ACKNOWLEDGEMENTS

The authors would like to thank for the financial supports from the National Natural Science Foundation of China (11272181, 11702133), the Tsinghua University Initiative Scientific Research Program (2014z09099), and the Natural Science Foundation of Jiangsu Province (BK20170772).

ORCID

Zhi Li http://orcid.org/0000-0003-2495-5816
Song Cen http://orcid.org/0000-0002-8674-4005
Yan Shang http://orcid.org/0000-0001-9869-5039

REFERENCES

1. Zienkiewicz OC, Taylor RL, Zhu JZ. *The Finite Element Method: Its Basis and Fundamentals*. 7th ed. Oxford, UK: Butterworth-Heinemann; 2013.
2. Long YQ, Cen S, Long ZF. *Advanced Finite Element Method in Structural Engineering*. Berlin, Germany: Springer-Verlag, Tsinghua University Press; 2009.
3. Wilson EL, Taylor RL, Doherty WP, Ghaboussi J. Incompatible displacement models. In: Fenves SJ, Perrone N, Robinson A, Schnobrich W, eds. *Numerical and Computer Methods in Structural Mechanics*. New York, NY: New York: Academic Press; 1973;43-57.
4. Taylor RL, Beresford PJ, Wilson EL. A non-conforming element for stress analysis. *Int J Numer Methods Eng*. 1976;10(6):1211-1219.
5. Abaqus. *Documentation*. Providence, RI: Dassault Systèmes Simulia Corp; 2017:2016.
6. Simo JC, Rifai MS. A class of mixed assumed strain methods and the mehod of incompatible modes. *Int J Numer Methods Eng*. 1990;29(8):1595-1638.
7. Pian THH, Sumihara K. Rational approach for assumed stress finite-elements. *Int J Numer Methods Eng*. 1984;20(9):1685-1695.
8. Chang-Chun W, Mao-Guang H, Pian THH. Consistency condition and convergence criteria of incompatible elements: general formulation of incompatible functions and its application. *Comput Struct*. 1987;27(5):639-644.
9. Yeo ST, Lee BC. New stress assumption for hybrid stress elements and refined four-node plane and eight-node brick elements. *Int J Numer Methods Eng*. 1997;40(16):2933-2952.
10. Sze KY. On immunizing five-beta hybrid-stress element models from 'trapezoidal locking' in practical analyses. *Int J Numer Methods Eng*. 2000;47(4):907-920.
11. Pian THH, Chang-Chun W. *Hybrid and Incompatible Finite Element Methods*. Boca Raton, FL: Chapman & Hall/CRC; 2006.
12. Cen S, Zhang T, Li C-F, Fu X-R, Long Y-Q. A hybrid-stress element based on Hamilton principle. *Acta Mech Sinica*. 2010;26(4):625-634.
13. Wanji C, Limin T. Isoparametric quasi-conforming element. *J Dalian Univ Tech*. 1981;20(1):63-74. (in Chinese)
14. Piltner R, Taylor RL. A quadrilateral mixed finite-element with two enhanced strain modes. *Int J Numer Methods Eng*. 1995;38(11):1783-1808.
15. Korelc J, Wriggers P. Improved enhanced strain four-node element with Taylor expansion of the shape functions. *Int J Numer Methods Eng*. 1997;40(3):407-421.
16. Lautersztajn-S N, Samuelsson A. Further discussion on four-node isoparametric quadrilateral elements in plane bending. *Int J Numer Methods Eng*. 2000;47(1-3):129-140.
17. Piltner R, Taylor RL. A systematic construction of B-bar functions for linear and non-linear mixed-enhanced finite elements for plane elasticity problems. *Int J Numer Methods Eng*. 1999;44(5):615-639.
18. Long Y, Li J, Long Z, Cen S. Area co-ordinates used in quadrilateral elements. *Commun Numer Methods Eng*. 1999;15(8):533-545.
19. Long Z, Li J, Cen S, Long Y. Some basic formulae for area co-ordinates in quadrilateral elements. *Int J Numer Methods Biomed Eng*. 1999;15(12):841-852.
20. Chen XM, Cen S, Long YQ, Yao ZH. Membrane elements insensitive to distortion using the quadrilateral area coordinate method. *Comput Struct*. 2004;82(1):35-54.
21. Cen S, Chen X-M, Fu X-R. Quadrilateral membrane element family formulated by the quadrilateral area coordinate method. *Comput Methods Appl Mech Eng*. 2007;196(41):4337-4353.
22. Cen S, Du Y, Chen X-M, Fu X-R. The analytical element stiffness matrix of a recent 4-node membrane element formulated by the quadrilateral area co-ordinate method. *Int J Numer Methods Biomed Eng*. 2007;23(12):1095-1110.
23. Du Y, Cen S. Geometrically nonlinear analysis with a 4-node membrane element formulated by the quadrilateral area coordinate method. *Finite Elem Anal Des*. 2008;44(8):427-438.
24. Chen X-M, Cen S, Fu X-R, Long Y-Q. A new quadrilateral area coordinate method (QACM-II) for developing quadrilateral finite element models. *Int J Numer Methods Eng*. 2008;73(13):1911-1941.
25. Cen S, Chen X-M, Li CF, Fu X-R. Quadrilateral membrane elements with analytical element stiffness matrices formulated by the new quadrilateral area coordinate method (QACM-II). *Int J Numer Methods Eng*. 2009;77(8):1172-1200.
26. Long Z-F, Cen S, Wang L, Fu X-R, Long Y-Q. The third form of the quadrilateral area coordinate method (QACM-III): theory, application, and scheme of composite coordinate interpolation. *Finite Elem Anal Des*. 2010;46(10):805-818.

27. Li G. A four-node plane parametric element based on quadrilateral area coordinate and its application to coupled solid-deformation/fluid-flow simulation for porous geomaterials. *Int J Numer Anal Methods Geomech*. 2015;39(3):251-276.
28. Macneal RH. A theorem regarding the locking of tapered four-noded membrane elements. *Int J Numer Methods Eng*. 1987;24(9):1793-1799.
29. Macneal RH. On the limits of finite element perfectability. *Int J Numer Methods Eng*. 1992;35(8):1589-1601.
30. Cen S, Zhou P-L, Li C-F, Wu C-J. An unsymmetric 4-node, 8-DOF plane membrane element perfectly breaking through MacNeal's theorem. *Int J Numer Methods Eng*. 2015;103(7):469-500.
31. Rajendran S, Liew KM. A novel unsymmetric 8-node plane element immune to mesh distortion under a quadratic displacement field. *Int J Numer Methods Eng*. 2003;58(11):1713-1748.
32. Felippa CA, Haugen B. A unified formulation of small-strain corotational finite elements: I. Theory. *Comput Methods Appl Mech Eng*. 2005;194(21-24):2285-2335.
33. Belytschko T, Liu W, Moran B, Elkhodary KI. *Nonlinear Finite Elements for Continua and Structures*. 2nd ed. Chichester, UK: John Wiley & Sons; 2014.
34. Hughes TJ, Winget J. Finite rotation effects in numerical integration of rate constitutive equations arising in large-deformation analysis. *Int J Numer Methods Eng*. 1980;15(12):1862-1867.
35. Rashid MM. Incremental kinematics for finite element applications. *Int J Numer Methods Eng*. 1993;36(23):3937-3956.
36. Simo JC, Hughes TJ. *Computational Inelasticity*. New York, NY: Springer Science & Business Media; 1998.
37. Wang C, Zhang X, Hu P, Qi Z. Linear and geometrically nonlinear analysis with 4-node plane quasi-conforming element with internal parameters. *Acta Mech Solida Sin*. 2015;28(6):668-681.
38. Ko Y, Lee P-S, Bathe K-J. A new 4-node MITC element for analysis of two-dimensional solids and its formulation in a shell element. *Comput Struct*. 2017;192:34-49.
39. Wisniewski K, Turska E. Improved 4-node Hu-Washizu elements based on skew coordinates. *Comput Struct*. 2009;87(7-8):407-424.
40. Wisniewski K, Wagner W, Turska E, Gruttmann F. Four-node Hu-Washizu elements based on skew coordinates and contravariant assumed strain. *Comput Struct*. 2010;88(21-22):1278-1284.
41. Zouari W, Hammadi F, Ayad R. Quadrilateral membrane finite elements with rotational DOFs for the analysis of geometrically linear and nonlinear plane problems. *Comput Struct*. 2016;173:139-149.
42. Wulfinghoff S, Bayat HR, Alipour A, Reese S. A low-order locking-free hybrid discontinuous Galerkin element formulation for large deformations. *Comput Methods Appl Mech Eng*. 2017;323:353-372.
43. Rajendran S, Zhang BR, Liew KM. Partition of unity-based 'FE-meshfree' QUAD4 element for geometric non-linear analysis. *Int J Numer Methods Eng*. 2010;82(12):1574-1608.
44. Cowan T, Coombs WM. Rotationally invariant distortion resistant finite-elements. *Comput Methods Appl Mech Eng*. 2014;275:189-203.
45. de Borst R, Crisfield MA, Remmers JJ, Verhoosel CV. *Nonlinear Finite Element Analysis of Solids and Structures*. 2nd ed. Chichester, UK: John Wiley & Sons; 2012.
46. Bathe KJ. *Finite Element Procedures*. 2nd ed. Watertown, MA: Klaus-Jürgen Bathe; 2014.
47. Battini J-M. A non-linear corotational 4-node plane element. *Mech Res Commun*. 2008;35(6):408-413.
48. Fredriksson M, Ottosen NS. Fast and accurate 4-node quadrilateral. *Int J Numer Methods Eng*. 2004;61(11):1809-1834.
49. Sze KY, Liu XH, Lo SH. Popular benchmark problems for geometric nonlinear analysis of shells. *Finite Elem Anal Des*. 2004;40(11):1551-1569.
50. Lyons P, Holsgrove S. *Finite Element Benchmarks for 2D Beams and Axisymmetric Shells Involving Geometric Non-Linearity*. Glasgow, UK: NAFEMS; 1989.
51. Cen S, Zhou G-H, Fu X-R. A shape-free 8-node plane element unsymmetric analytical trial function method. *Int J Numer Methods Eng*. 2012;91(2):158-185.
52. Zhou P-L, Cen S, Huang J-B, Li C-F, Zhang Q. An unsymmetric 8-node hexahedral element with high distortion tolerance. *Int J Numer Methods Eng*. 2017;109(8):1130-1158.

How to cite this article: Li Z, Cen S, Wu C-J, Shang Y, Li C-F. High-performance geometric nonlinear analysis with the unsymmetric 4-node, 8-DOF plane element US-ATFQ4. *Int J Numer Methods Eng*. 2018;114:931–954. https://doi.org/10.1002/nme.5771

APPENDIX A: THE SECOND FORM OF QUADRILATERAL AREA COORDINATES (QACM-II)

As shown in Figure A1, M_i ($i = 1,2,3,4$) are the midside points of element edges $\overline{23}$, $\overline{34}$, $\overline{41}$, and $\overline{12}$, respectively. Then, the position of an arbitrary point P within the quadrilateral element $\overline{1234}$ can be uniquely specified by area coordinates S and T (QACM-II), which are defined as

$$S = 4\frac{\Omega_1}{A}, \quad T = 4\frac{\Omega_2}{A}, \tag{A.1}$$

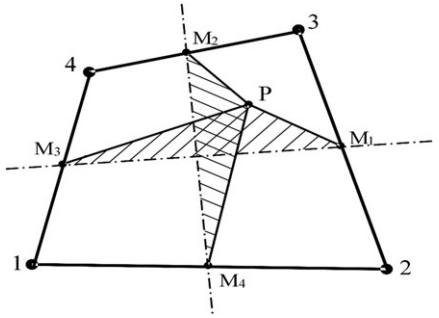

FIGURE A1 Definition of the quadrilateral area coordinates S and T of QACM-II[24]

where A is the area of the quadrilateral element; and Ω_1 and Ω_2 are the generalized areas of ΔPM_2M_4 and ΔPM_3M_1, respectively. The values of generalized areas Ω_1 and Ω_2 can be both positive and negative: for ΔPM_2M_4 (or ΔPM_3M_1), if the permutation order of points P, M_2, and M_4 (or P, M_3, and M_1) is anticlockwise, a positive Ω_1 (or Ω_2) should be taken; otherwise, Ω_1 (or Ω_2) should be negative.

Two shape parameters $\bar{g}_1$ and $\bar{g}_2$ are defined here as

$$\begin{cases} \bar{g}_1 = \frac{A_{\Delta 123} - A_{\Delta 124}}{A} \\ \bar{g}_2 = \frac{A_{\Delta 234} - A_{\Delta 123}}{A} = \frac{A - A_{\Delta 124} - A_{\Delta 123}}{A}, \end{cases} \tag{A.2}$$

in which $A_{\Delta 123}$, $A_{\Delta 124}$, and $A_{\Delta 234}$ are the areas of $\Delta 123$, $\Delta 124$, and $\Delta 234$, respectively. Different values of these shape parameters mean different shapes of a quadrangle. Thus, the local coordinates of the corner nodes and midside points can be written as

$$\begin{aligned} &\text{node}\,1 : (S_1, T_1) = \left(-1 + \bar{g}_2, -1 + \bar{g}_1\right); \quad \text{node}\,2 : (S_2, T_2) = \left(1 - \bar{g}_2,\ \ 1 - \bar{g}_1\right); \\ &\text{node}3 : (S_3, T_3) = \left(1 + \bar{g}_2,\ \ 1 + \bar{g}_1\right); \qquad \text{node}\,4 : (S_4, T_4) = \left(-1 - \bar{g}_2, -1 - \bar{g}_1\right); \\ &\quad M_1 : (1,\ \ 0); \qquad\qquad\qquad\qquad M_2 : (0,\ \ 1); \\ &\quad M_3 : (-1,\ \ 0); \qquad\qquad\qquad\qquad M_4 : (0, -1). \end{aligned} \tag{A.3}$$

The aforementioned coordinate values are only small modifications for isoparametric coordinates, ie,

$$\begin{cases} S = \xi + \bar{g}_2 \xi\eta \\ T = \eta + \bar{g}_1 \xi\eta \end{cases} \tag{A.4}$$

Moreover, the relationship between QACM-II and the Cartesian coordinates is

$$\begin{cases} S = \frac{1}{A}\left[(a_3 - a_1) + (b_3 - b_1)x + (c_3 - c_1)y\right] + \bar{g}_1 = \frac{1}{A}\left[\bar{a}_1 + \bar{b}_1 x + \bar{c}_1 y\right] + \bar{g}_1 \\ T = \frac{1}{A}\left[(a_4 - a_2) + (b_4 - b_2)x + (c_4 - c_2)y\right] + \bar{g}_2 = \frac{1}{A}\left[\bar{a}_2 + \bar{b}_2 x + \bar{c}_2 y\right] + \bar{g}_2 \end{cases}, \tag{A.5}$$

where

$$\begin{cases} \bar{a}_1 = a_3 - a_1, \quad \bar{b}_1 = b_3 - b_1, \quad \bar{c}_1 = c_3 - c_1, \\ \bar{a}_2 = a_4 - a_2, \quad \bar{b}_2 = b_4 - b_2, \quad \bar{c}_2 = c_4 - c_2, \end{cases} \tag{A.6}$$

$$\begin{aligned} &a_i = x_j y_k - x_k y_j, \quad b_i = y_j - y_k, \quad c_i = x_k - x_j, \\ &(i = 1, 2, 3, 4, \quad j = 2, 3, 4, 1, \quad k = 3, 4, 1, 2) \end{aligned} \tag{A.7}$$

in which (x_i, y_i) $(i = 1, 2, 3, 4)$ are the Cartesian coordinates of the 4 corner nodes.

APPENDIX B: THE EXPRESSIONS OF $\left[{}^{t}\hat{\mathbf{N}}\right]$ IN EQUATION (14)

${}^{t}U_7$, ${}^{t}V_7$, ${}^{t}U_8$, and ${}^{t}U_8$ in Equation (11) are the linear displacement solutions or plane pure bending in arbitrary direction and referred to configuration C_1. For isotropic case, they can be written as[29]

$$\begin{cases} {}^{t}U_7 = \frac{3}{16E'A^3}\left[\left(4\bar{c}_1^2\bar{c}_2A - \bar{c}_1^2\bar{b}_2f_3 - \bar{b}_1\bar{b}_2^2f_1 - 16\bar{b}_1\mu'A^2\right)^{t}S^2 + 2\bar{b}_2\bar{f}_1^2{}^{t}S^{t}T - \bar{b}_1f_1^{2t}T^2\right] \\ {}^{t}V_7 = \frac{3}{16E'A^3}\left[\left(4\bar{b}_1^2\bar{b}_2A - \bar{b}_1^2\bar{c}_2f_3 - \bar{c}_1\bar{c}_2^2f_1 - 16\bar{c}_1\mu'A^2\right)^{t}S^2 + 2\bar{c}_2f_1^{2t}S^{t}T - \bar{c}_1f_1^{2t}T^2\right], \end{cases} \tag{B.1}$$

$$\begin{cases} {}^{t}U_8 = \frac{3}{16E'A^3}\left[-\bar{b}_2f_2^{2t}S^2 + 2\bar{b}_1f_2^{2t}S^{t}T - \left(4\bar{c}_2^2\bar{c}_1A + \bar{c}_2^2\bar{b}_1f_3 + \bar{b}_2\bar{b}_1^2f_2 + 16\bar{b}_2\mu'A^2\right){}^{t}T^2\right] \\ {}^{t}V_8 = \frac{3}{16E'A^3}\left[-\bar{c}_2f_2^{2t}S^2 + 2\bar{c}_1f_2^{2t}S^{t}T - \left(4\bar{b}_2^2\bar{b}_1A + \bar{b}_2^2\bar{c}_1f_3 + \bar{c}_2\bar{c}_1^2f_2 + 16\bar{c}_2\mu'A^2\right){}^{t}T^2\right], \end{cases} \tag{B.2}$$

where ${}^{t}S$ and ${}^{t}T$ are the quadrilateral area coordinates at time t.

Furthermore, $\left[{}^{t}\hat{\mathbf{N}}\right]$ in Equation (14) can be rewritten as[29]

$$\left[{}^{t}\hat{\mathbf{N}}\right] = [\mathbf{P}]\left[{}^{t}\hat{\mathbf{d}}\right]^{-1}, \tag{B.3}$$

where

$$\left[{}^{t}\hat{\mathbf{d}}\right] = \begin{bmatrix} \mathbf{P}\left({}^{t}x_1\,{}^{t}y_1\,{}^{t}S_1\,{}^{t}T_1\right) \\ \mathbf{P}\left({}^{t}x_2\,{}^{t}y_2\,{}^{t}S_2\,{}^{t}T_2\right) \\ \mathbf{P}\left({}^{t}x_3\,{}^{t}y_3\,{}^{t}S_3\,{}^{t}T_3\right) \\ \mathbf{P}\left({}^{t}x_4\,{}^{t}y_4\,{}^{t}S_4\,{}^{t}T_4\right) \end{bmatrix} = \begin{bmatrix} 1 & 0 & {}^{t}x_1 & 0 & {}^{t}y_1 & 0 & U_7\left({}^{t}S_1\,{}^{t}T_1\right) & U_8\left({}^{t}S_1\,{}^{t}T_1\right) \\ 0 & 1 & 0 & {}^{t}x_1 & 0 & {}^{t}y_1 & V_7\left({}^{t}S_1\,{}^{t}T_1\right) & V_8\left({}^{t}S_1\,{}^{t}T_1\right) \\ 1 & 0 & {}^{t}x_2 & 0 & {}^{t}y_2 & 0 & U_7\left({}^{t}S_2\,{}^{t}T_2\right) & U_8\left({}^{t}S_2\,{}^{t}T_2\right) \\ 0 & 1 & 0 & x_2 & 0 & y_2 & V_7\left({}^{t}S_2\,{}^{t}T_2\right) & V_8\left({}^{t}S_2\,{}^{t}T_2\right) \\ 1 & 0 & {}^{t}x_3 & 0 & {}^{t}y_3 & 0 & U_7\left({}^{t}S_3\,{}^{t}T_3\right) & U_8\left({}^{t}S_3\,{}^{t}T_3\right) \\ 0 & 1 & 0 & {}^{t}x_3 & 0 & {}^{t}y_3 & V_7\left({}^{t}S_3\,{}^{t}T_3\right) & V_8\left({}^{t}S_3\,{}^{t}T_3\right) \\ 1 & 0 & {}^{t}x_4 & 0 & {}^{t}y_4 & 0 & U_7\left({}^{t}S_4\,{}^{t}T_4\right) & U_8\left({}^{t}S_4\,{}^{t}T_4\right) \\ 0 & 1 & 0 & {}^{t}x_4 & 0 & {}^{t}y_4 & V_7\left({}^{t}S_4\,{}^{t}T_4\right) & V_8\left({}^{t}S_4\,{}^{t}T_4\right) \end{bmatrix}, \tag{B.4}$$

in which $({}^{t}x_I, {}^{t}y_I)$ and $({}^{t}S_I, {}^{t}T_I)$ are respectively the Cartesian coordinates and quadrilateral area coordinates (QACM-II) of the 4 corner nodes ($I = 1, 2, 3, 4$) at time t; and $[\mathbf{P}]$ has been given by Equation (11).